Computers in Biology and Medicine 209 (2026) 111695

Contents lists available at ScienceDirect

Computers in Biology and Medicine

journal homepage: www.elsevier.com/locate/compbiomed

Novel velocity model for the quantitative characterization of pleural sliding, in vivo multicenter clinical study on RF lung ultrasound data

Chiara Zangrandi [a], Federico Mento [a], Mattia Perpenti [a], Giovanni Pierro [b], Alessandro Perrotta [b], Tiziano Perrone [c], Andrea Smargiassi [b], Riccardo Inchingolo [b,1,2], Libertario Demi [a,2,*]

[a] Department of Information Engineering and Computer Science, University of Trento, Trento, 38123, Italy
[b] Fondazione Policlinico Universitario Agostino Gemelli IRCCS, Rome, 00168, Italy
[c] Department of Internal Medicine, Humanitas Gavazzeni, Bergamo, 24125, Italy

HIGHLIGHTS

- We propose a novel methodology to estimate the velocity of pleural sliding, inspired by functional ultrasound (fUS).
- The proposed methodology was evaluated on two datasets, comprising five different pathological populations.
- The estimated sliding velocities were within the physiological range.
- Statistical analysis and binary classification highlighted the diagnostic potential of this feature.

ARTICLE INFO

Keywords:
Functional ultrasound
Lung sliding
Pleural sliding
Quantitative lung ultrasound
Sliding velocity

ABSTRACT

Quantitative lung ultrasound (LUS) has emerged as a way to improve current LUS data analysis, based on the visual interpretation of imaging patterns. However, most studies on quantitative LUS have neglected dynamic imaging patterns. Among these, pleural sliding is well-known for its clinical relevance, but few studies have focused on its quantitative characterization. Therefore, in this study, we introduce a novel methodology to estimate the velocity of pleural sliding inspired by functional ultrasound (fUS). Additionally, we assessed, through binary classifiers, the potential of this feature in distinguishing between lung pathologies. We applied the methodology to two *in-vivo* datasets, comprising multifrequency RF data acquired from patients affected by cardiogenic pulmonary edema (CPE), pneumonia, COPD, fibrosis, and exacerbated. Specifically, we analyzed a total of 536 multifrequency LUS videos from 79 patients. The resulting sliding velocity values were within the physiological range (≈0.49 mm/s - ≈ 4.39 mm/s). Among all pathological populations, COPD was characterized by the minimum velocity and pneumonia by the maximum velocity, on average. The statistical analysis highlighted some statistically significant differences, especially when comparing COPD with the other pathologies. These differences were confirmed also with binary classifiers that showed accuracies up to 94.06% (when differentiating between COPD and pneumonia). These results demonstrate the potential of this novel methodology to extract clinically valuable information and highlight its applicability in future diagnostic processes.

1. Introduction

Lung ultrasound (LUS) is a non-invasive imaging technique that offers many advantages, such as safety, bedside availability, cost-effectiveness, and real-time imaging [1,2]. These advantages make it suitable also for resource-limited environments and emergency situations, such as pandemic scenarios [3]. However, LUS does not enable direct anatomical representation of the lung because air disrupts the propagation of ultrasound waves beyond the pleural line [1,3]. The analysis

* Corresponding author.
Email address: libertario.demi@unitn.it (L. Demi).
[1] Co-last author.
[2] These authors contributed equally to this work.

https://doi.org/10.1016/j.compbiomed.2026.111695
Received 19 December 2025; Received in revised form 7 April 2026; Accepted 16 April 2026
Available online 25 April 2026

of LUS videos is therefore limited to the visual interpretation of imaging patterns, which is highly subjective and leads to qualitative analysis [1].

Recent studies have been focusing on quantitative approaches as a way to overcome this limitation. Specifically, these approaches focus on extracting quantitative features to characterize imaging patterns. These features demonstrate differentiating potential [1,4,5], showing that they could be used as relevant parameters during the diagnostic process. However, most studies on quantitative LUS focus only on the static aspect of imaging patterns, neglecting valuable information that could be obtained from dynamic features.

A well-known dynamic imaging pattern is pleural sliding, also called lung sliding. This pattern can be identified as a lateral movement of the pleural line and is thought to be caused by the two pleural layers sliding on each other [6]. Pleural sliding can be found in most of the LUS videos since it is an indication of aeration of the lung at the site of the probe placement on the chest wall [1]. The relevance of this pattern is already well-established, since its absence indicates a pathological case that affects lung compliance and/or regional ventilation [7]. For example, Lichtenstein et al. [8] demonstrated that pneumothorax is characterized by the absence of pleural sliding. Moreover, Via et al. [9] reported some qualitative variations in the velocity of pleural sliding across different pathologies. However, the qualitative assessment of these variations limits the reproducibility and accuracy of the results.

Only a few studies have focused on the quantitative characterization of pleural sliding, both in terms of amplitude and velocity [7,10–17]. Lichtenstein et al. [10] proposed a simple technique based on the manual measurement of the amplitude of pleural sliding, obtained by measuring the displacement of some reference points. This technique was also used in Şirin et al. [11] to analyze the pleural sliding of LUS data acquired from mechanically ventilated patients. However, the identification of the reference point is not straightforward, especially on healthy lungs where no irregularities are present, and the manual measurement of pleural sliding remains characterized by high subjectivity. Alternatively, two automated techniques have been developed to quantify this pattern: respectively based on Doppler ultrasound and Speckle tracking.

The application of Doppler ultrasound to LUS data was proposed by Rose et al. [12]. Specifically, they implemented tissue Doppler and qualitatively demonstrated that it could distinguish between present or abolished pleural sliding. Xiao et al. [13] also applied tissue Doppler on data acquired from patients with unilateral pneumothorax. They reported values of ≈3.8 mm/s for the pneumothorax side and ≈5.9 mm/s for the non-pneumothorax side. Briganti et al. [7] used both a pulse wave Doppler to estimate the velocity of pleural sliding and a manual measurement to estimate the amplitudes on B-mode data. The pleural sliding velocities estimated were ≈10.3 cm/s at the apex and ≈13.9 cm/s at the base.

Dori and Jakobson [18] first hypothesized the application of speckle tracking to pleural sliding quantification. This technique was used by Duclos et al. [14] and by Fissore et al. [15] to distinguish between cases of pneumothorax and non-pneumothorax. They reported results in terms of maximal pleural strain and demonstrated the diagnostic potential of this feature when considering pneumothorax cases. Duclos et al. [16] also applied the same speckle tracking technique to a dataset of healthy volunteers. In this case, they highlighted greater lung motion in the posterior area than in the anterior one. Speckle tracking was also used by Tzadok et al. [17] to differentiate between Covid-19, acute decompensated heart failure (ADHF), and non-respiratory complaint patients. They found a significant increase in velocity in ADHF patients (≈3.4 mm/s), followed by Covid-19 patients (≈1.4 mm/s), and patients with non-respiratory complaints (≈0.2 mm/s).

However, the proposed approaches are based on existing techniques developed for other applications and they might not be optimal for LUS data. For example, speckle tracking is not applicable at the pleural interface or within the lung region because a fully formed speckle pattern cannot be assumed to exist in these areas. Additionally, Doppler ultrasound is angle dependent, and velocity measurement at 90° is not possible. However, most of the LUS acquisitions are obtained with the probe at a 90° angle with respect to the pleural line. Therefore, even if these techniques provide some insightful results, a proper characterization of pleural sliding may benefit from the development of a dedicated methodology.

Furthermore, most of these studies [12–15] and proposed deep-learning techniques [19,20] focused merely on identifying the presence or absence of pleural sliding to diagnose pneumothorax. The characterization of this imaging pattern in other pathologies and in healthy lungs remains to be thoroughly investigated.

This paper aims to quantify pleural sliding by introducing a novel methodology inspired by functional ultrasound (fUS) [21]. Specifically, we developed a velocity model that correlates the velocity of pleural sliding, the sliding velocity (SlV), to the frequency content of the slow-time intensity (STI) signals. Additionally, within a multicenter clinical study, we assess the potential of SlV to distinguish five different pathologies: cardiogenic pulmonary edema (CPE), pneumonia (PNE), chronic obstructive pulmonary disease (COPD), pulmonary fibrosis (PF), and pulmonary fibrosis exacerbation (PFE).

The rest of the paper is organized as follows. In Section 2, the methodology is explained in detail. The results are shown in Section 3 and discussed in Section 4. Finally, Section 5 summarizes the conclusions.

2. Methods

2.1. Dataset

In this study, we analyzed pathological data of four different pathologies: CPE, pneumonia, COPD, and fibrosis. These pathologies have been chosen because of their social and clinical impact [3]. Indeed, fibrosis has a high mortality rate [22], which worsens when the pathology progresses to acute exacerbation [23]. Moreover, COPD and other respiratory infections, such as pneumonia, were reported among the leading causes of death worldwide in 2021 [24].

In this study, we consider patients affected by a worsening condition of fibrosis, fibrosis exacerbated, as a different population. In total, we therefore evaluated five pathological populations from two different datasets: LUSARD dataset and SAURON dataset. The acquisition process of the two datasets followed similar protocols, and the harmonization of the different probes was guaranteed by the equalized pressure outputs. Both the protocol and harmonization process are described in Refs. [4,5]. For both datasets, patients were in a sitting position and asked to breathe normally for the entire length of the acquisition. No mechanical ventilation was used.

The LUSARD dataset was acquired at the Emergency and Urgency department of Humanitas Gavazzeni (Bergamo, Italy) within the context of the lung ultrasound for acute respiratory disease study. The study was approved by the independent ethics committee for clinical studies of IRCCS clinical institute Humanitas of Rozzano: protocol number 553/21. The dataset is described in details in Mento et al. [4]. Radio frequency (RF) data were acquired using an Ultrasound Advanced Open Platform (ULA-OP)[25] and a linear probe (LA533, Esaote, Florence, Italy: 192 elements, 245 μm pitch). Data were acquired with a multifrequency approach (center frequencies of 3, 4, 5, 6 MHz), with a sampling frequency of 50 MHz. A speed of sound of 1546 m/s was assumed for the time-to-space conversion. A subaperture of 64 elements was implemented for both transmission phase and reception phase, forming images of 129 lines. A different number of cycles for each center frequency was set to guarantee a pulse length of 2 μs for all center frequencies. The pulse repetition frequency (PRF) was 4 kHz, resulting in a frame rate of 31 Hz (PRF/#lines = 4000/129). If we consider only frames of the same center frequency, the actual frame rate is obtained by dividing by the number of center frequencies, in this case equal to 31/4 = 7.75 Hz. The focal point was set at 2 cm, depth at which, on average, the pleural line is found. At the focal point, the −12 dB lateral resolution was measured to be 0.81, 0.66, 0.65, and 0.54 mm at the center frequency of 3, 4, 5, and 6 MHz, respectively [4]. Each patient was scanned in 12 different areas

as described in Mento et al. [4] and according to the protocol described in Soldati et al. [26]. Specifically, these 12 areas were chosen from the acquisition protocol, including all the areas except the mid-posteriors (areas 2 and 5). However, it is important to note that, due to the aim for which this dataset was acquired, data were collected for a given area only if vertical artifacts and consolidations were detected. Data were acquired from 28 patients: 13 affected by pneumonia (8 males and 5 females, with ages ranging from 51 to 90 with an average of 72.6 years) and 15 affected by CPE (8 males and 7 females, with ages ranging from 48 to 91 with an average of 79.7 years). The diagnoses were derived with standard clinical examinations, e.g., computed tomography (CT).

The SAURON dataset was acquired at Fondazione Policlinico Universitario Agostino Gemelli (Rome, Italy) and approved by the Ethical Committee of the Fondazione Policlinico Universitario Gemelli IRCCS in Rome, protocol 0002865/22, ID 4710. The dataset is described in detail in Perpenti et al. [5]. Data were acquired using an ULA-OP research scanner [25] connected to a linear probe (LA523, Esaote, Florence, Italy: 192 elements, 245 μm pitch). Each patient was scanned in 10 different areas as described in Perpenti et al. [5] and according to the protocol described in Soldati et al. [26]. Specifically, these 10 areas were selected from the acquisition protocol, including all the areas except the mid-posterior (areas 2 and 5) and the upper-lateral (areas 8 and 10). The reduction from 12 to 10 areas was decided in order to simplify the acquisition process, as it has been demonstrated that this reduction does not compromise the quality of the analysis [27]. In this dataset, all areas were acquired regardless of the presence of a specific LUS pattern. Imaging settings and parameters were consistent with the ones used for the LUSARD dataset. Data were acquired from 51 patients: 19 affected by COPD (13 males and 6 females between 45 and 79 years with an average age of 68.2 years), 20 affected by fibrosis (14 males and 6 females between 46 and 88 years with an average age of 73.6 years) and 12 affected by fibrosis exacerbation (8 males and 4 females between 54 and 87 years with an average age of 72.4 years). The diagnoses were derived with standard clinical examinations, e.g., computed tomography (CT).

In total we analyzed 536 multifrequency videos: 60 videos of patients affected by CPE (LUSARD dataset), 41 videos of pneumonia (LUSARD dataset), 154 videos of COPD (SAURON dataset), 172 videos of fibrosis (SAURON dataset), and 109 videos of exacerbated fibrosis (SAURON dataset). Each video consisted of 23 multifrequency frames, where each multifrequency frame comprises 4 frames of the same region acquired with 4 different center frequencies.

2.2. Velocity model

In this study, we developed a methodology to estimate the SIV. The core part of this methodology is a velocity model that we developed inspired by the fUS technique idea, introduced by Mace et al. [21]. The idea is that moving scatterers within the field of view (FOV) introduce some variation in the slow-time intensity (STI) signal of the corresponding pixels on the B-mode Ultrasound data. Faster scatterers cause faster intensity variations, which means STI signals with higher frequency components.

Furthermore, focusing only on one pixel, as shown in Fig. 1, a moving scatterer has an influence on its STI signal only when crossing within an interaction length. This length is determined by the lateral extent of the ultrasound beam, i.e., by the lateral resolution.

Based on this idea, we developed the velocity model to estimate the 'pixel velocity' (v_p), defined as the velocity of a scatterer moving within the interaction length and causing variations in the STI signal corresponding to that pixel. The velocity model is based on two assumptions. The first assumption is that the sliding velocity and the frequency component of the STI signal are indeed related, while the second assumption is that the SIV only has a lateral component. We developed the velocity model starting from two boundary cases, representing the minimum and maximum estimable velocities. The minimum velocity is assumed to be equal to zero. Indeed, a stationary scatterer within the interaction length does not induce any intensity variation in the STI signal, whose frequency domain therefore consists only of a DC component ($f = 0$).

On the other hand, the maximum estimable velocity occurs in the case of a scatterer moving across the interaction length in one sampling time (t_s) (Fig. 2). The maximum velocity of the scatterer is then simply calculated as the interaction length (equal to the lateral resolution) divided by the sampling time. Moreover, the sampling time is the inverse of the sampling frequency (f_s), therefore the velocity can be calculated as follows:

$$v_{max} = \frac{res_{lat}}{t_s} = res_{lat} \ * \ f_s, \tag{1}$$

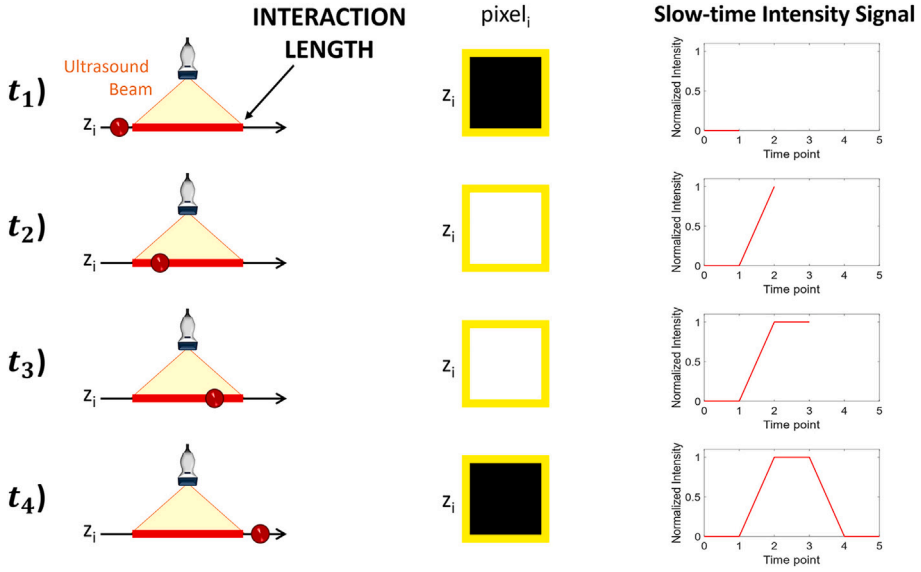

Fig. 1. In this figure, a scatterer (red circle) is moving in space at a certain depth z_i and in time from time point t_1 to time point t_4. The intensity of the i_{th} pixel at the z_i depth is influenced by the scatterer only when the latter interacts with the ultrasound beam (at t_2 and t_3). The length of this interaction is determined by the beam profile, and it is therefore set to be equal to the lateral resolution.

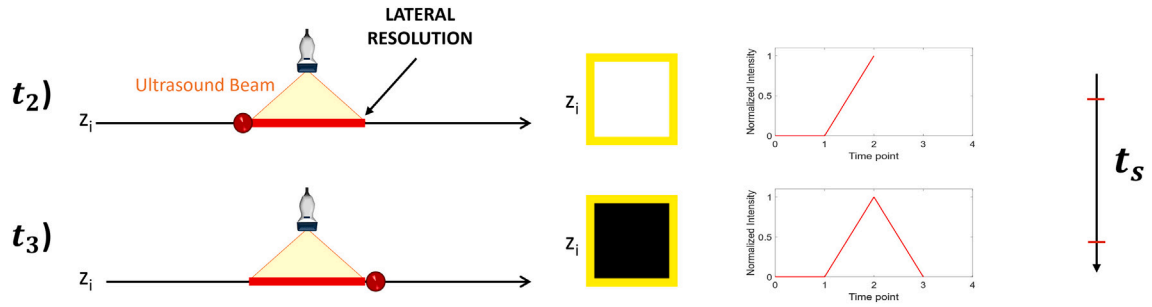

Fig. 2. This figure illustrates the case of the maximum estimable velocity. In this case a scatterer (red circle) is interacting with the ultrasound beam only in one sample (t_2). This means that in a sampling time (t_s), from t_2 to t_3, the scatterer crosses a length equal to the lateral resolution.

where res_{lat} is the lateral resolution, t_s is the sampling time, and f_s the sampling frequency. However, for this velocity estimates, we are considering STI signals, whose frequency domain gives unique content within the range $[0, \frac{f_s}{2}]$. Therefore, being $f_{max} = \frac{f_s}{2}$, the maximum velocity can be expressed as:

$$v_{max} = res_{lat} * 2f_{max}. \tag{2}$$

The velocity model is then defined assuming a linear relation between the frequency and the velocity, and it is as follows:

$$v_p = res_{lat} * 2f_p, \tag{3}$$

res_{lat} being the lateral resolution at -12 dB, and f_p being the pixel frequency defined as the frequency with the highest amplitude in the power spectral density (PSD) of the STI signal.

2.3. Sliding velocity estimation process

The developed methodology estimates one SIV value for each video. The process is divided into three parts, as illustrated in Fig. 3. In the first part (Fig. 3(i)), the region of interest (ROI) for the SIV estimation is selected. The second part (Fig. 3(ii)) implements the proposed velocity model and estimates the pixel velocity of each pixel within the ROI. In the third part (Fig. 3(iii)), the SIV value is estimated.

Specifically, the ROI selection (Fig. 3(i)) is implemented not only to focus the analysis on the relevant region of the image (pleural line), but also to ensure sufficient signal quality by applying an intensity threshold. To this end, an average intensity image is obtained by computing the temporal average across the frames of the video. Then, an intensity threshold of −12 dB is applied to the average intensity image and a binary mask is obtained. This threshold is chosen for consistency, as lateral resolution is estimated at the same intensity. This choice is further supported by a sensitivity analysis at −6, −12, and −18 dB, performed on the clinical data from the LUSARD and SAURON datasets, with correlations and linear regression evaluated for three pairs: −6 vs −12 dB, −12 vs −18 dB, and −6 vs −18 dB.

In parallel, the pleural line is automatically segmented using the Automatic Segmentation Algorithm of the Pleural Line (ASAP), described in detail in Perpenti et al. [5]. Finally, the ROI is defined as the intersection of the two masks.

The second part (Fig. 3(ii)) estimates the pixel velocity. Specifically, the following steps are implemented for each pixel within the ROI. First, the power spectral density (PSD) of the STI signal is estimated. Specifically, for each STI signal, the mean value is removed to eliminate the DC component. A Hamming window with a length equal to the full signal length (23 samples) is applied. The PSD is estimated using Welch's method, implemented via the *pwelch* function in MATLAB. The Fast Fourier transform length (NFFT) is set to twice the signal length, resulting in zero-padding of the signal. Therefore, the apparent frequency resolution is equal to 0.168 Hz ($\Delta f_a = f_s/2N = 0.168\ Hz$, with f_s = 7.75 Hz, and N = 23 $samples$), which is half the theoretical frequency resolution of 0.337.

Second, from the PSD, the pixel frequency (f_p) is selected as the frequency at which the PSD shows the maximum amplitude. Third, the pixel frequency is used in the velocity model to estimate the pixel velocity.

Finally, the SIV is estimated (Fig. 3(iii)) as the mean of the pixel velocities within the ROI, according to the following equation:

$$SIV = \frac{1}{N}\sum_{i=1}^{N} v_{p_i}, \tag{4}$$

where $(v_p)_i$ is the velocity of the i-th pixel, and N is the total number of pixels within the ROI (with $v_p > 0$).

2.4. Experimental validation

We conducted an experimental validation of the proposed sliding velocity estimation process. Data were acquired using the same imaging parameters and settings as those described for clinical acquisitions in Section 2.1. Specifically, data were acquired with the ULA-OP research platform [25] and the LA533 (Esaote, Florence, Italy) linear probe. The experimental setup consisted of a pleural phantom made of austenitic stainless steel AISI (American Iron and Steel Institute) 316L (Euronorm number 1.4404) [28] positioned on a support and immersed in a water tank. The linear probe was fixed on an automatic positioning system (GAMPT, Merseburg, Germany) at 2 cm above the phantom. The automatic positioning system was programmed to move laterally over the phantom at a set velocity. In total, data were acquired at 10 different velocities, summarized in Table 1. Since the automatic positioning system only allows velocity selection as percentages of its maximum speed (18.75 mm/s), we chose percentages based on the expected velocity range of our proposed model and we included higher velocities to test the saturation effect.

2.5. Statistical analysis

We performed an agreement analysis to investigate whether SIV depends on the center frequency or represents an independent physical quantity. To this end, we conducted a frequency agreement analysis across all six frequency pairs (3–4, 3–5, 3–6, 4–5, 4–6, and 5–6 MHz). For each pair, we computed both Pearson correlation coefficients and Bland-Altman analyses.

We then conducted a statistical analysis to assess differences between each pathological population (cardiogenic pulmonary edema (CPE), pneumonia (PNE), chronic obstructive pulmonary disease (COPD), fibrosis (PF), and fibrosis exacerbated (PFE)). Specifically, we investigated five different cases and conducted the analyses for each of the ten possible population pairs (CPE-PNE, CPE-COPD, CPE-PF, CPE-PFE, PNE-COPD, PNE-PF, PNE-PFE, COPD-PF, COPD-PFE, PF-PFE) and for each center frequency (3 MHz, 4 MHz, 5 MHz, 6 MHz), resulting in a total of 40 analyses per case (10 pairs × 4 center frequencies).

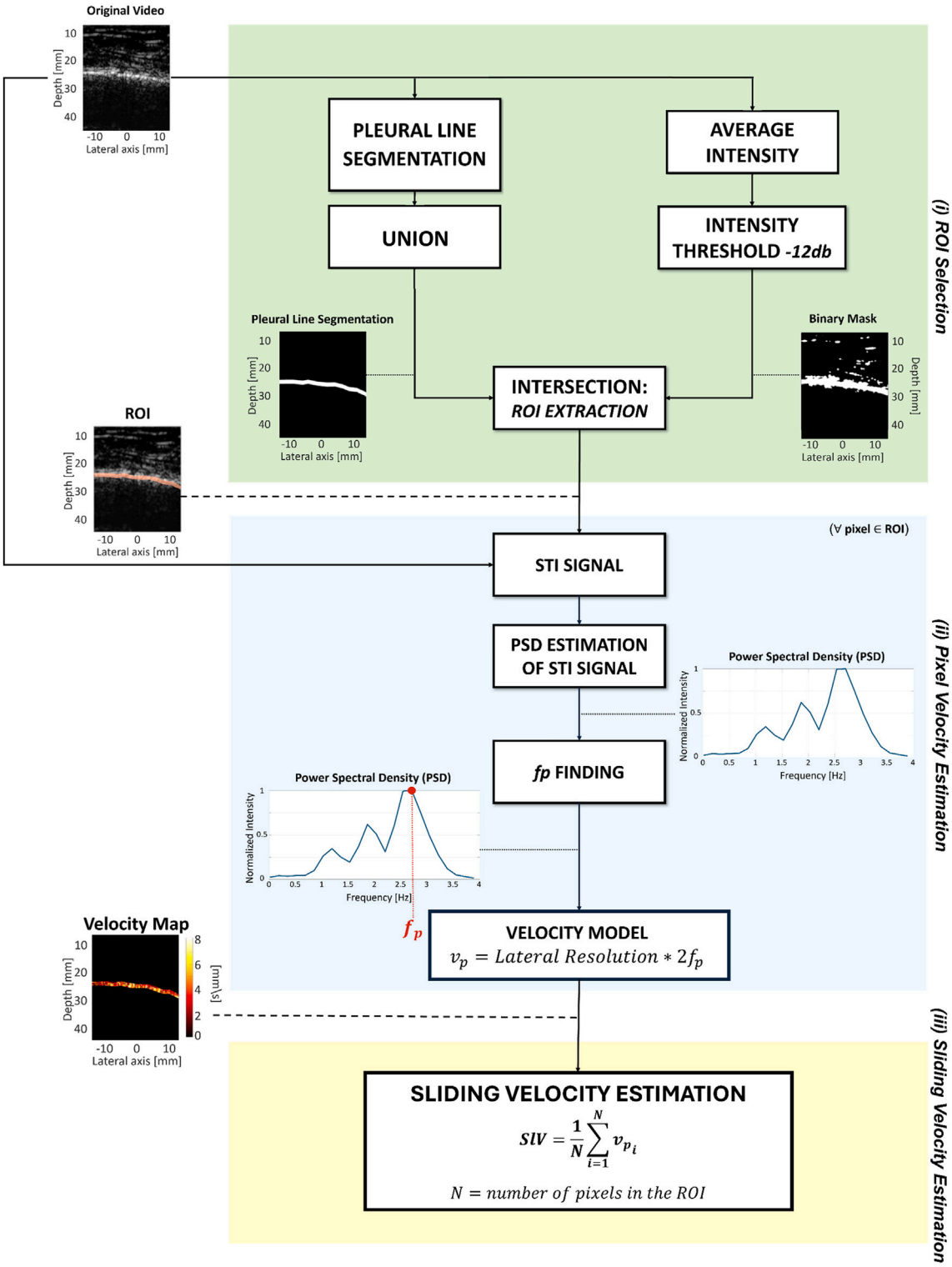

Fig. 3. This figure illustrates the block diagram of the sliding velocity estimation process. The process is divided into three parts. In (i), the ROI for the sliding velocity estimation is extracted. The ROI is defined as the intersection between the pleural line segmentation and the binary mask obtained by thresholding the original data. In (ii), the v_p of the pixels within the ROI are estimated using the velocity model described in Section 2.2. In (iii), the SIV is estimated as the mean of the pixel velocities within the ROI.

In the first case, we analyzed all estimated SIV values and applied a linear mixed-effects model to address the dependence between SIV values of the same patient. In particular, we considered the pathology as a fixed effect and the patient ID as a random effect, using the model:

$$SIV_{ij} = \beta_0 + \beta_1\ pathology_i + b_i + \epsilon_{ij}, \tag{5}$$

where SIV_{ij} is the observed value for patient i and zone j, β_0 is the global intercept, β_1 is the fixed effect of the pathology, b_i is the

Table 1
In this table, the velocities used for the phantom experimental validation are reported as percentages of the maximum speed of the automatic positioning system and the corresponding velocities.

Percentage [%]	1	5	10	15	20	25	30	40	60	100
Velocity [mm/s]	0.19	0.56	0.94	1.88	3.75	4.69	5.63	7.50	11.25	18.75

random intercept for patient i, and ε_{ij} is the residual error for zone j of patient i.

We also estimate the effect size for each pair by calculating the standardized mean difference, defined as the estimated difference divided by the estimated residual variance, both provided by the model outputs. The 95% confidence intervals (CI) were calculated using ±1.96 standard errors.

In the other cases, analyses were performed only at the patient level, meaning that in each population we consider only one value per patient. Specifically, in the second case, we consider the mean of SIV values across the different LUS videos of each patient. In the third and fourth cases, we consider the minimum and the maximum SIV values of each patient, respectively. In the fifth case, we consider the delta SIV value of each patient, calculated as the difference between the minimum SIV value and the maximum SIV value of each patient. In each case, we tested the five populations for normality using the Shapiro-Wilk test [29]. Then, we performed pairwise statistical analyses for each center frequency. We chose to analyze all pair comparisons using the Mann–Whitney U test [30] for consistency, as most populations were not normally distributed. We then estimated the effect size of all tests with the rank-biserial correlation, and we reported the 95% CI, calculated using ±1.96 standard errors.

Finally, all p-values were corrected using the Benjamini–Hochberg method to control the false discovery rate (FDR). All tests assumed an alpha (α) value of 0.05. All statistical analyses were performed on the clinical data from the LUSARD and SAURON datasets.

2.6. Classifiers

The performance of SIV in discriminating lung diseases was tested through standard binary classifiers. Specifically, we selected four SIV features at the patient level as in the statistical analysis (mean SIV, minimum SIV, maximum SIV, delta SIV). Moreover, the tests were performed for ten pairs of diseases, as described in the statistical analysis, (CPE-PNE, CPE-COPD, CPE-PF, CPE-PFE, PNE-COPD, PNE-PF, PNE-PFE, COPD-PF, COPD-PFE, PF-PFE).

For each pair, four types of standard binary classifiers were utilized: Naive Bayes, Decision Tree, Support Vector Machine (SVM), and k-Nearest Neighbors (KNN) by means of the MATLAB functions *"fitcnb"*, *"fitctree"*, *"fitcsvm"*, and *"fitcknn"* (with *"MinParentSize"* set to 10), respectively.

To detect the most significant set of features, for each pair of diseases we trained $2^4 - 1$ classifiers, each one with a possible combination of input features [combinations of 1 input feature (4) + combinations of 2 input features (6) + combinations of 3 input features (4) + combinations of 4 input features (1), for a total of 15 combinations]. All the combinations were trained with the same cross validation, consisting of a nested K-fold strategy, with both outer and inner folds equal to 3. Hyperparameters were optimised in the inner fold, always with a balanced number of patients from each class, and then tested in the outer fold. To avoid partitioning bias, this procedure was repeated 10 times. Performances were described by three classification metrics (CMs): accuracy, sensitivity, and specificity. For each CM distribution, minimum, mean, and maximum values were extracted to describe the model performance. This testing process was computed four times, one for each center frequency.

Finally, the highest mean accuracy, corresponding to a specific configuration of a classifier, a center frequency, and a feature combination, was selected to describe the overall classification performance for each pathological pair. In these cases, confusion matrices, receiver operating characteristic (ROC) curves and area under the curve (AUC) values were estimated. Specifically, ROC curves and AUC values were obtained with the $perfcurve$ function in MATLAB. Each confusion matrix was computed as the mean of the 10 confusion matrices (one for each repetition) and then normalized by the sample size of the corresponding pathology.

3. Results

The maximum estimable pixel velocity for each center frequency is, respectively, 6.28, 5.12, 5.04, and 4.19 mm/s for 3, 4, 5, and 6 MHz. An example of velocity maps estimated for each center frequency is reported in Fig. 4.

In Table 2, the results of the sensitivity analysis for the three different thresholds (−6, −12, and −18 dB) are reported. Specifically, Pearson correlation coefficients and linear regression slopes are presented for each threshold pair at each center frequency.

In Fig. 5, the results of the experimental validation are shown. Specifically, Fig. 5 shows the correlation between estimated SIV values and the real velocities in [mm/s]. Samples are represented by circles and connected with lines to visualize the trend in the data.

In Figs. 6 and 7, and Table 3, we report the results of the frequency agreement analysis. Specifically, Fig. 6 shows the correlation for all six

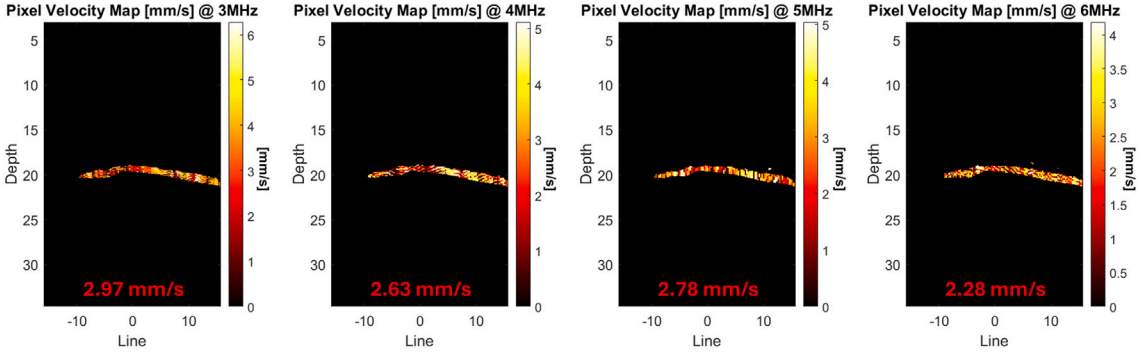

Fig. 4. This figure shows four velocity maps, one for each center frequency. Each pixel in the ROI is color-coded based on its individual pixel velocity. The corresponding SlV value is numerically reported in red above each figure.

Table 2
In this table, the results of the sensitivity analysis for the intensity threshold are reported. Specifically, the Pearson coefficients are shown in the first three columns and the linear regression slopes in the last three. Each column represents an intensity pair, and each row represents a center frequency.

Freq	Pearson coefficient			Linear regression slope		
[MHz]	−6 vs −12 [dB]	−12 vs −18 [dB]	−6 vs −18 [dB]	−6 vs −12 [dB]	−12 vs −18 [dB]	−6 vs −18 [dB]
3	0.905	0.976	0.876	0.746	0.931	0.690
4	0.883	0.970	0.855	0.688	0.943	0.647
5	0.849	0.973	0.815	0.684	0.956	0.646
6	0.832	0.970	0.803	0.665	0.977	0.646

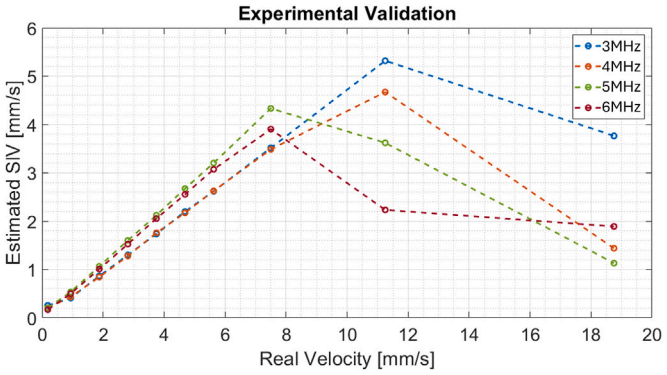

Fig. 5. This figure shows the correlation between estimated SIV values and the real velocities measured during the experimental validation, both in [mm/s]. Individual samples are marked with a circle, while the connecting lines highlight the trend in the data.

frequency pairs. The Pearson correlation coefficient for each pair is indicated in the top-left corner of the corresponding plot. The results of Bland-Altman analyses are reported in Fig. 7 and Table 3. Specifically, Fig. 7 shows the Bland-Altman plots for each frequency pair. The mean difference across all data points is represented by a continuous red line, whereas the 95% limits of agreement (LoA) are represented by dashed red lines. Table 3 reports numerically the mean difference and the LoA values for each frequency pair.

In Fig. 8, the estimated SIV values are reported in four plots, one for each center frequency. In each plot, the distribution of SIV values for each pathological population is shown with a violin plot. The median velocity of each population is shown numerically beneath each violin, reported in [mm/s]. Fig. 9 shows the differences between the minimum SIV values and maximum SIV values, estimated at a patient level as described in Section 2.5. Specifically, each violin plot reports the distribution of minimum SIV values on the left side and the distribution of maximum SIV values on the right side.

The results of the statistical analysis are reported in the Appendix A (See Appendix A in Tables A.4–A.8). The results of the linear mixed-effects model for case 1 are presented in Table A.4. The results of the Mann-Whitney tests for cases 2, 3, 4, and 5 are reported in Tables A.5–A.8. Each table, for each pathological pair and for each center frequency, shows: the p-values obtained from the statistical analysis, the adjusted q-values obtained from the FDR correction, the effect size computed as the standardized mean difference for case 1 and rank-biserial correlation for the other cases, and the 95% CI. Statistically significant results are highlighted in yellow (α <0.05).

Figs. 10 and 11 show the classification results. Specifically, one plot for each pathological pair is reported. Each plot is divided into four sections, one for each center frequency. In each section, only the best performing classifier is reported. For each classifier, the classification metrics are reported in different colors: accuracy in blue, sensitivity in red, and specificity in green. The percentage of the accuracy is numerically shown next to the corresponding classification metric. The normalized confusion matrices are reported in the Appendix B (See Appendix B Figs. B.12–B.14). The ROC curves and the AUC values are reported in the Appendix C (See Appendix C Figs. C.15 and C.16).

All the reported results are obtained from clinical data from LUSARD and SAURON datasets, except for Fig. 5, which reports data from the experimental validation.

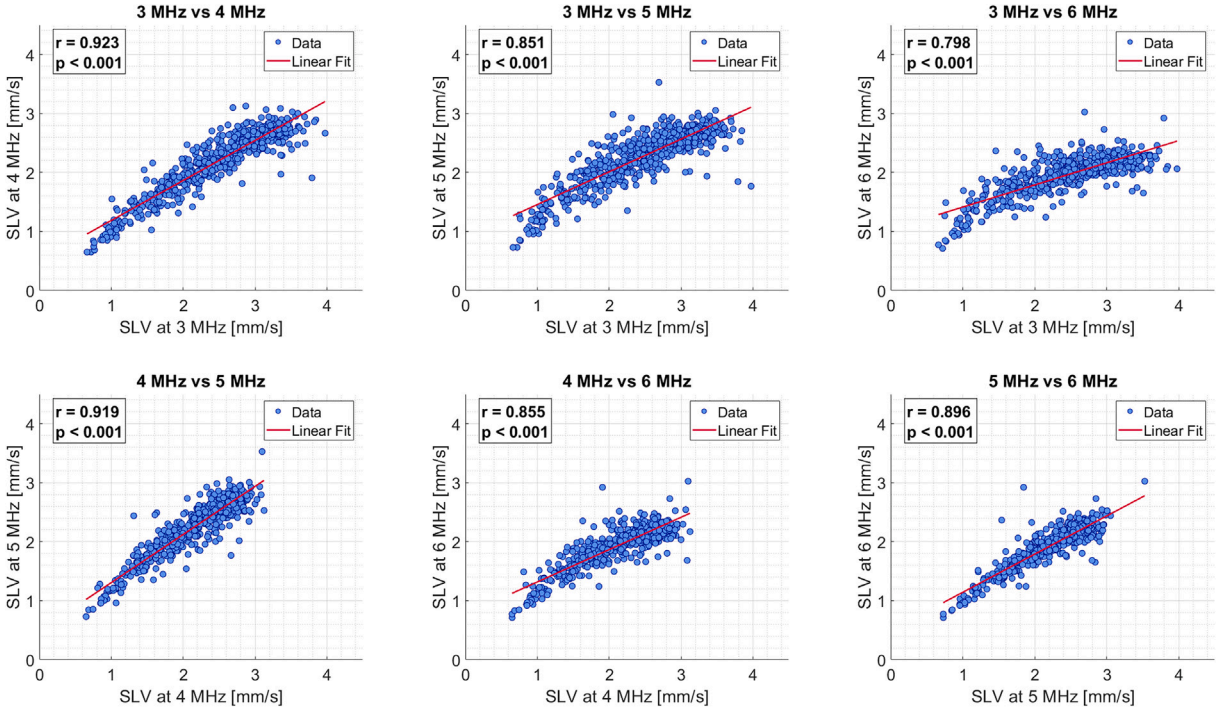

Fig. 6. This figure shows the correlation for all six frequency pairs, with the Pearson correlation coefficient indicated in the top-left corner of each pair plot. Each sample is marked as a blue dot, and the linear interpolation across all the data is shown as a red line.

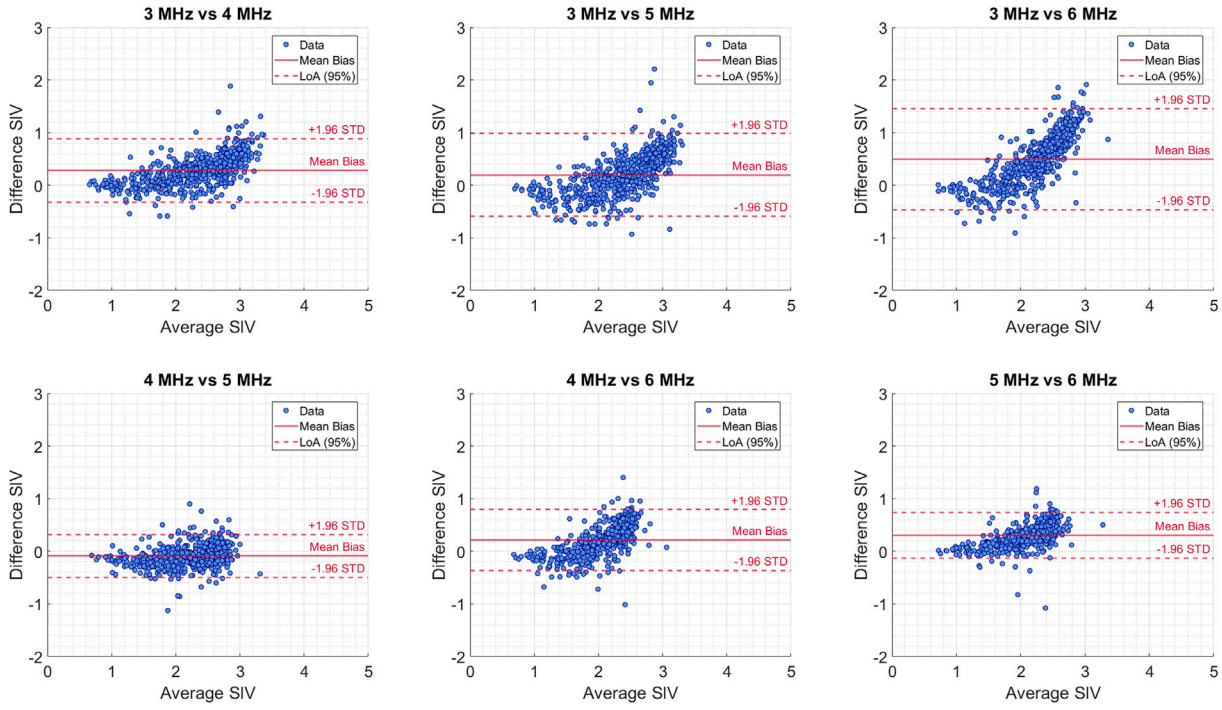

Fig. 7. This figure shows the results of Bland-Altman analysis. Six plots are reported, one for each frequency pair. The mean difference across all data points is represented by a continuous red line. The 95% limits of agreement (LoA) are reported as dashed red lines.

Table 3
In this table, the mean difference and the LoA values are reported for each frequency pair.

	3–4 [MHz]	3–5 [MHz]	3–6 [MHz]	4–5 [MHz]	4–6 [MHz]	5–6 [MHz]
Mean Difference [mm/s]	0.285	0.195	0.499	−0.089	0.215	0.304
LoA (95%)	[−0.315 0.884]	[−0.591 0.981]	[−0.460 1.458]	[−0.496 0.317]	[−0.362 0.791]	[−0.130 0.738]

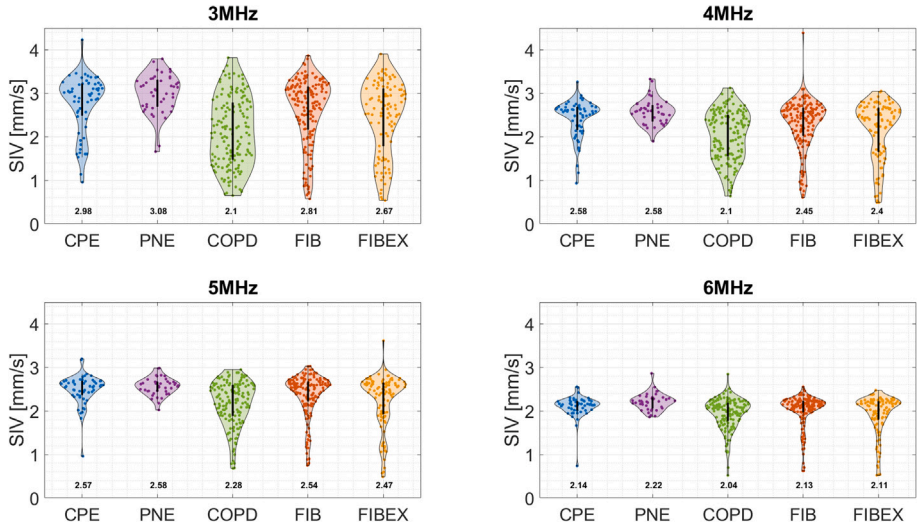

Fig. 8. This figure reports the estimated SIV values in four plots, one for each center frequency. The violin plots show the distribution of SIV values for each pathological population. The median velocity of each population is shown numerically beneath each violin, reported in [mm/s].

4. Discussion

First, we perform a sensitivity analysis to support the choice of the threshold at −12 dB. The results are shown in Table 2. Overall, Pearson coefficients confirm a strong correlation, ranging from 0.803 to 0.976 ($p<0.001$). Linear regression shows the stronger agreement for −12 vs −18 dB pair with a slope nearly equal to 1 (0.93–0.98), while the other comparisons, involving −6 dB, show lower slopes (0.65–0.75). This effect may be caused by a reduction of pixels within the ROI. Considering the strong agreement with adjacent thresholds, −12 dB is kept as the reference threshold.

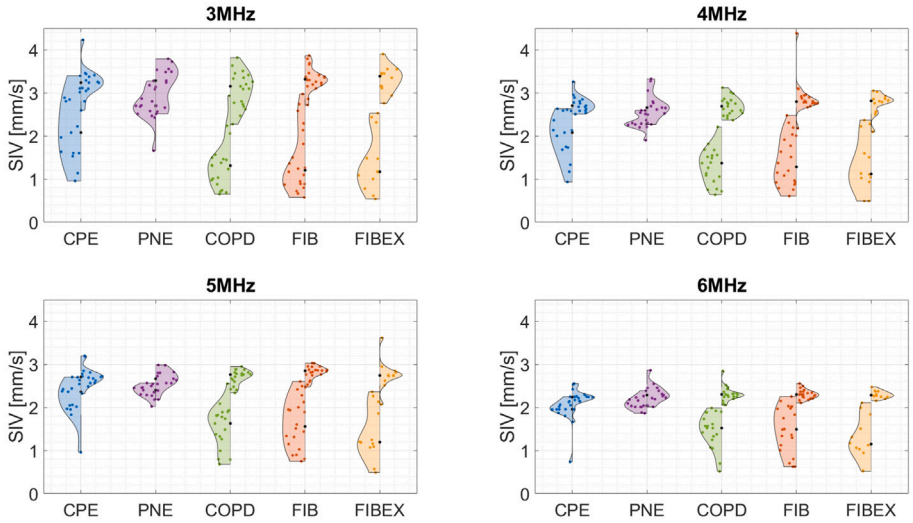

Fig. 9. This figure presents four plots, one for each center frequency. In each plot, the distribution of minimum SIV values and maximum SIV values is shown for each pathological population. Specifically, the left and right sides of each violin respectively report the distribution for minimum and maximum SIV values.

The results of experimental validation, shown in Fig. 5, demonstrate a strong linear correlation between the estimated SIV values and the real velocities within the range 0 to ≈7 mm/s. For higher velocities, the correlation is no longer linear. A possible explanation is that the model reaches its maximum estimable velocity, introducing a saturation effect. Furthermore, Fig. 5 shows a steeper slope for higher center frequencies (5 and 6 MHz), demonstrating greater accuracy in the velocity estimation. However, these frequencies are characterized by a narrower velocity range compared to lower frequencies (3 and 4 MHz). Indeed, the latter are less accurate, but show larger velocity ranges as predicted by the model.

The frequency agreement analysis is then implemented on each frequency pair to investigate the dependency of the SIV on the center frequency. The correlation plots (Fig. 6) show a strong correlation among each frequency. As expected, the pairs of closer frequencies (3–4, 4–5, and 5–6 MHz) show higher Pearson coefficients (r = 0.923, 0.919, and 0.896), while the most distant pair (3–6 MHz) shows the lowest correlation (r = 0.798). While this could suggest a frequency dependency of SIV, it is important to note that it might also be caused by the mentioned saturation effect, as described in the model. Indeed, maximum estimable velocity decreases with increasing center frequency. Therefore, higher velocities that are correctly mapped at 3 MHz may be incorrectly estimated at 6 MHz, reducing the correlation of the pair. This phenomenon is also highlighted in the Bland–Altman analysis, which shows the presence of a proportional bias on the higher part of the velocities (Fig. 7 and Table 3). Indeed, the differences between measurements at lower velocity ranges (0 to ≈ 2 mm/s) are centered around zero, indicating a good agreement. However, the difference increases as the mean velocity increases, showing a proportional bias.

The distributions of SIV values for the five pathologies for each center frequency are shown in Fig. 8. Generally speaking, all distributions report SIV values within the physiological range (≈0.49 mm/s - ≈ 4.39 mm/s). These values are also in line with the velocities estimated by Tzadok et al. [17] (≈0.2 mm/s - ≈ 3.4 mm/s) and Xiao et al. [13](≈3.8 mm/s - ≈ 5.9 mm/s). Moreover, as the center frequency increases from 3 MHz to 6 MHz, the median velocity of all populations decreases. This was expected since the velocity model used to estimate the pixel velocity includes the lateral resolution, which depends on the center frequency. Indeed, higher center frequency means better lateral resolution, which means smaller lateral resolution values and therefore lower velocity values. This also has an impact on the maximum velocity estimable for each center frequency, whereas the minimum estimable velocity is always equal to zero. Therefore the distributions are narrower at higher center frequencies, as we see from Fig. 8. The inconsistency of the 5 MHz data in following this trend may be caused by the very small difference in lateral resolution between 4 MHz and 5 MHz (approximately 0.01 mm), which is likely too small to produce an appreciable effect.

If we focus on the comparison of the pathological distributions in Fig. 8, we see that differences between populations are present. Specifically, COPD is the population with consistently the lowest median value for all center frequencies. On the contrary, pneumonia is the population with the highest median value for all center frequencies. However, this might be influenced by the fact that this population has the smallest amount of data. This observation could be addressed in future work by increasing the size of the dataset, which may result in a broader distribution.

Fibrosis and fibrosis exacerbated populations show similar distributions, as they are representative of different stages of the same pathology. However, it is interesting to note that the acute stage (fibrosis exacerbated) has a slightly lower median value in all center frequencies. Additionally, these two distributions are also similar to the CPE, especially at higher frequencies.

Fig. 9 shows minimum and maximum SIV values for each pathology for each center frequency. Minimum SIV values distributions are much broader than the maximum SIV value distributions. This may indicate a saturation problem, meaning that the maximum estimable SIV value is too low, causing higher velocities to be underestimated by the proposed estimation process. Indeed, the datasets used in this study were originally designed for static pattern analysis, and the frame rate at which data were acquired (7.75 Hz) is not optimised for our application. Future work should focus on investigating the role played by the frame rate in the estimation of SIV, and on assessing the optimal value of this parameter.

The statistical analysis results show statistically significant differences among the populations. The results of case 1 (total data) and case 2 (mean), in Table A.4 and in Table A.5, are similar and both highlight a pronounced difference between COPD and the other pathologies, but fibrosis is exacerbated. Indeed, in case 1, the adjusted q-values show statistically significant differences, confirmed by the magnitude of the effect size, between COPD and fibrosis at 3 and 4 MHz (effect sizes of 0.64 and 0.50), COPD and CPE at 3, 4, and 5 MHz (effect sizes of −0.90, −0.75 and −0.66), and COPD and pneumonia at all frequencies (effect sizes of −1.19, −1.04, −0.79 and −0.75).

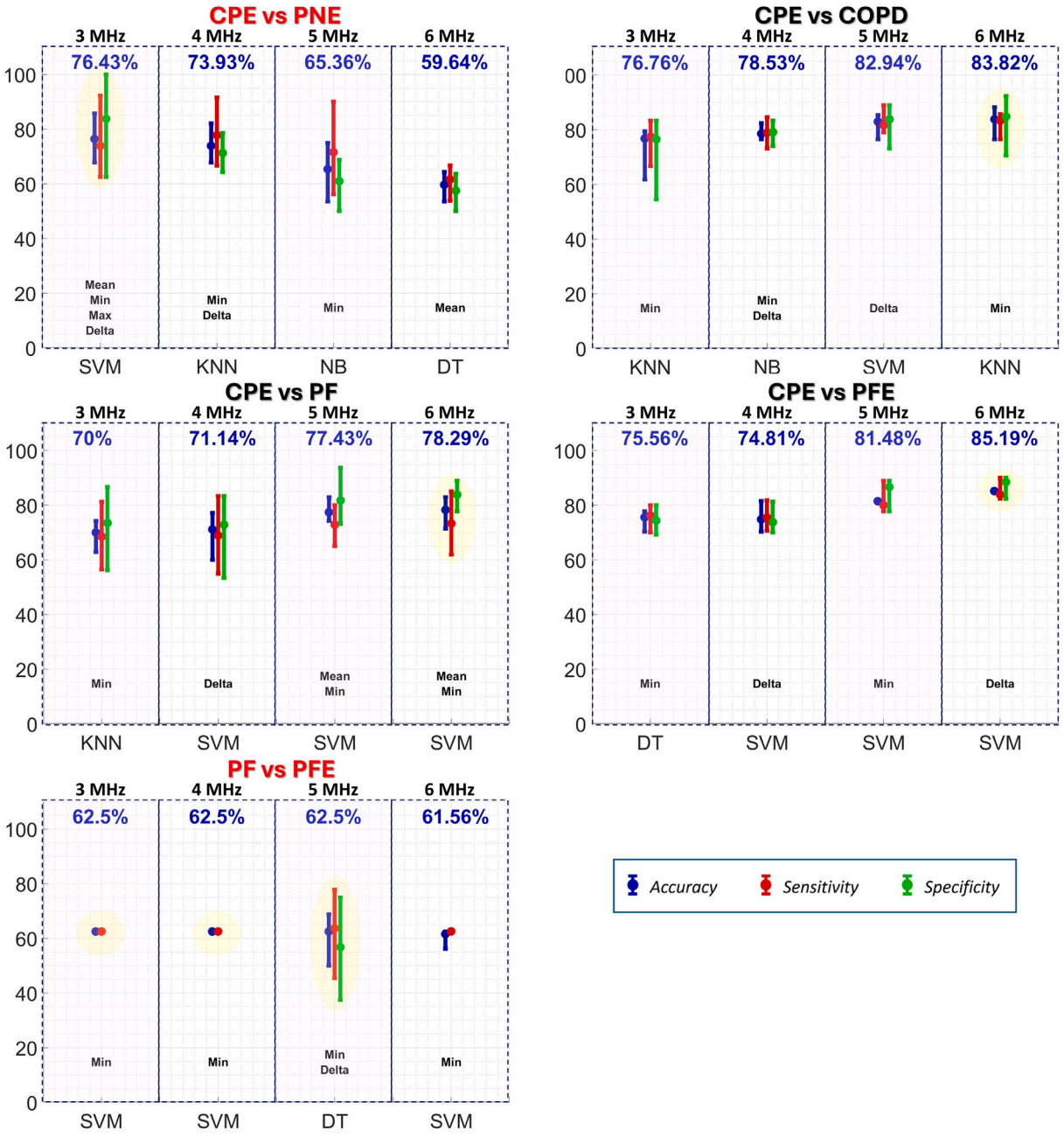

Fig. 10. This figure reports the classification results for five pathological pairs: CPE-PNE, CPE-COPD, CPE-PF, CPE-PFE, PF-PFE, where CPE stands for cardiogenic pulmonary edema, PNE for pneumonia, COPD for chronic obstructive pulmonary disease, PF for fibrosis, and PFE for fibrosis exacerbation. This figure shows five plots, one for each pathological pair. Each plot is divided into four boxes, one for each center frequency. The classification metrics reported in each box are accuracy (in blue), sensitivity (in red), and specificity (in green). The numerical value of the accuracy is shown next to the corresponding classification metric. Only the best performing classifier for the pathological pairs for each center frequency is shown. The feature or combination of features used for each classifier is shown above each classifier name. Pairs of pathologies within the same dataset are highlighted in red.

Case 3 (minimum) and Case 5 (delta), in Table A.6 and in Table A.8, highlight the differences between pneumonia and COPD, fibrosis, and fibrosis exacerbated. Indeed, compared to the other populations (Fig. 8), the pneumonia distribution is consistently narrower across all frequencies and is shifted toward higher velocities. However, as we already noted, this finding may be biased by differences in the amount of data from the pneumonia population compared to the others.

Case 4 (maximum), in Table A.7, reports very few significant differences, according to the p-value, and none with the q-value. This may be further evidence of the previously mentioned saturation problem. Low maximum estimable velocity leads to less accurate characterization of higher velocities.

Finally, the similarity between fibrosis and fibrosis exacerbated populations, as noted in Fig. 8, is confirmed in the statistical analysis with high p-values across all five cases, as shown in Table A.4–A.8.

The results from binary classifiers (Figs. 10 and 11) indicate no specific center frequency nor classifier emerges as consistently having the best results.

When differentiating between CPE and pneumonia (Fig. 10), comparable accuracies are obtained at 3 MHz with the SVM classifier

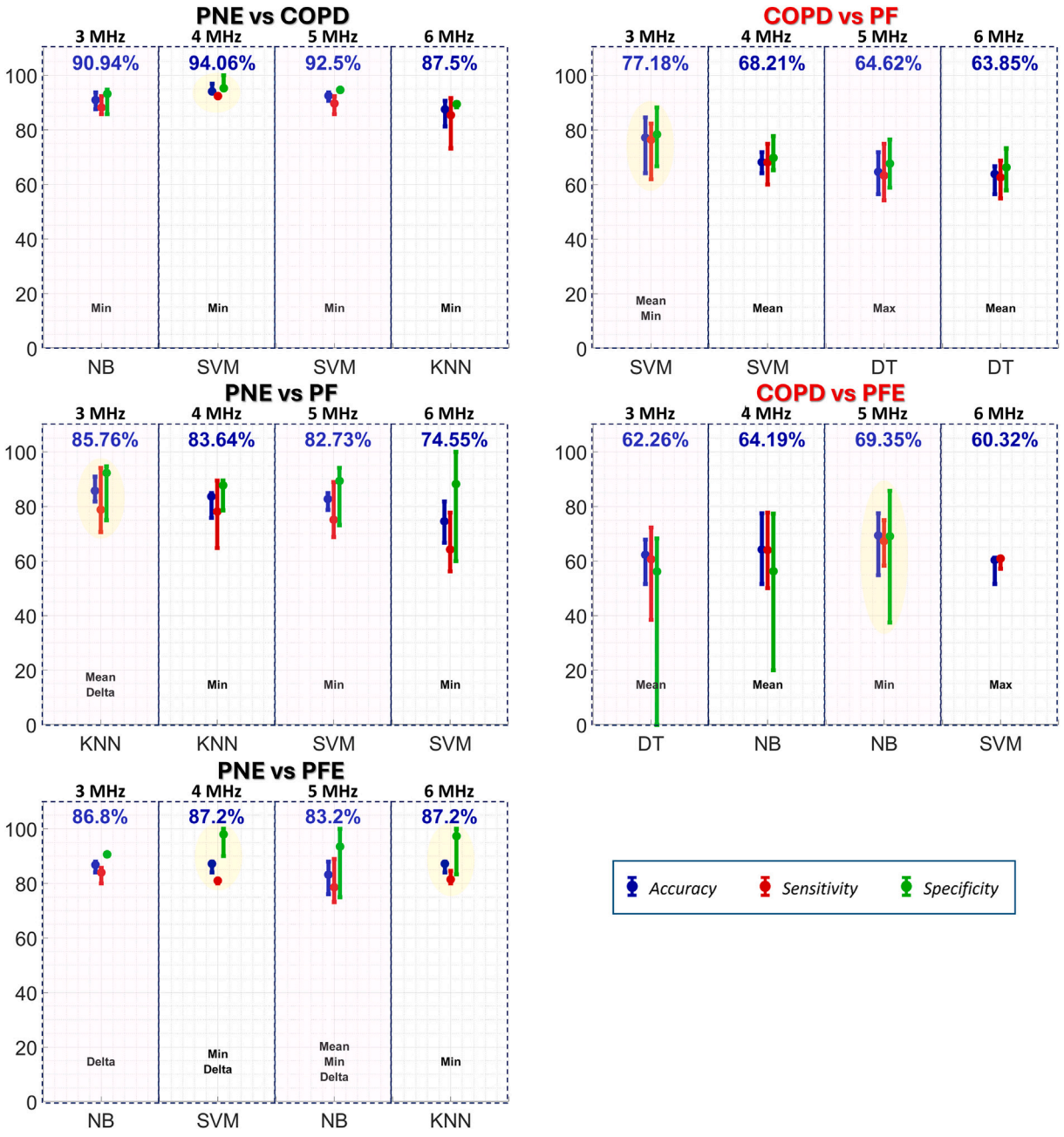

Fig. 11. This figure reports the classification results for five pathological pairs: PNE-COPD, PNE-PF, PNE-PFE, COPD-PF, COPD-PFE, where PNE stands for pneumonia, COPD for chronic obstructive pulmonary disease, PF for fibrosis, and PFE for fibrosis exacerbated. This figure shows five plots, one for each pathological pair. Each plot is divided into four boxes, one for each center frequency. The classification metrics reported in each box are accuracy (in blue), sensitivity (in red), and specificity (in green). The numerical value of the accuracy is shown next to the corresponding classification metric. Only the best performing classifier for the pathological pairs for each center frequency is shown. The feature or combination of features used for each classifier is shown above each classifier name. Pairs of pathologies within the same dataset are highlighted in red.

(76.43%) and at 4 MHz with the KNN classifier (73.93%). However, KNN shows slightly more balanced sensitivity, demonstrating robustness in differentiating between the two pathologies.

The differentiation between CPE and COPD (Fig. 10) shows high accuracy at 6 MHz using a KNN classifier (83.82%). However, the sensitivity and specificity at 4 MHz are slightly more balanced, indicating strong robustness in the classification process, even if the accuracy is slightly lower (78.53%).

Fig. 10 shows that high accuracies are also obtained when differentiating between CPE and fibrosis (78.29% at 6 MHz using an SVM classifier), and CPE and exacerbated fibrosis (85.19% at 6 MHz using an SVM classifier).

Classification between fibrosis and fibrosis exacerbated (Fig. 10) shows the poorest results, often failing to distinguish between the two populations and instead classifying both as fibrosis (as shown in the confusion matrices in Fig. B.12). This finding is particularly interesting because these populations, as we mentioned, represent the same pathology at different stages, as already noted and seen in Fig. 8.

As shown in Fig. 11, the best classification result is obtained when differentiating between pneumonia and COPD reaching an accuracy as

high as 94.06% at 4 MHz with the SVM classifier. The balanced sensitivity and specificity prove the robustness of this differentiation. This difference is also highlighted by the confusion matrix shown in Fig. B.14 and by the high AUC value (0.95), shown in Fig. C.16. These results confirm the differences between these two populations, as noted from Fig. 8. Indeed, COPD has the lowest median value and pneumonia the highest one.

Fig. 11 shows that high classification accuracy is also achieved when distinguishing pneumonia from the two fibrotic populations (fibrosis and fibrosis exacerbated). Specifically, an accuracy of 85.76% is achieved at 3 MHz with a KNN classifier when distinguishing between pneumonia and fibrosis. Whereas, an accuracy of 87.20% is achieved at 4 MHz with a SVM classifier and at 6 MHz with a KNN classifier when distinguishing between pneumonia and fibrosis exacerbated.

Finally, the best accuracy (77.18%) when differentiating between fibrosis and COPD (Fig. 11) is achieved at 3 MHz with an SVM classifier. Interestingly, a lower accuracy (69.35%) is achieved when differentiating between COPD and the worsening of fibrosis, fibrosis exacerbation (Fig. 11), with an NB classifier at 5 MHz.

Finally, it is important to acknowledge several limitations of this study that may introduce bias into the final results. For example, the choice of assuming the PSD peak as representative of the SIV in the velocity model (Section 2.2) may introduce errors. Indeed, the PSD peak may reflect not only the velocity of a laterally moving object but also other factors, such as out-of-plane motion. Future work will focus on better understanding the implications of this choice and evaluating alternative approaches. Moreover, variability of the PSD peak is also introduced by the fact that the PSD estimates are inherently noisy due to the very limited number of samples for each STI signal (23 frames). Future work will focus on increasing the number of frames to improve reliability and stability.

Another important limitation, as already mentioned, is the relatively low frame rate, which may cause the saturation effect discussed above. Although none of the SIV values, shown in Fig. 8, reaches the maximum estimable velocity, some individual pixel velocities do reach this limit, as shown in Fig. 4. This behavior is to be expected, since SIV is calculated as the mean of all pixel velocities within the ROI, and the presence of lower pixel velocities reduces the overall SIV values. Further investigation into this effect is needed to better characterize the proposed velocity model.

A significant limitation identified during the experimental validation is that although there is a strong linear correlation between the estimated SIV and the real velocity, this relation is not characterized by a unitary slope. Instead, the estimated values appear to be scaled by a factor of ≈2 with respect to the real velocity, and this underestimation could be due to the averaging operation in the sliding velocity formula. This suggests that SIV should be interpreted as an instrument-specific motion biomarker, rather than an absolute velocity. Future work will focus on investigating this dependence and evaluating the scaling factor of 2 to determine whether the process needs a generalized calibration or a more targeted approach.

It is also important to note that, since diagnoses do not overlap across datasets, binary classification between diseases from different datasets may be influenced by site-specific characteristics. Specifically, there are four pairs with pathologies from the same dataset (CPE-PNE, COPD-PF, COPD-PFE, PF-PFE). The results from other pathological pairs (CPE-COPD, CPE-PF, CPE-PFE, PNE-COPD, PNE-PF, PNE-PFE) should be interpreted as exploratory.

Further, the two datasets were acquired using slightly different strategies, i.e., 10 areas were scanned for SAURON and 12 for LUSARD, which might have introduced a bias in the results. Indeed, the pathological populations differ in the amount of available data and, therefore, classification results obtained from pairs of different datasets have inherent limitations. Moreover, the acquired videos were not synchronized with a specific breathing phase, and no additional metadata were acquired during the acquisition (such as respiratory rate, PEEP, tidal volumes). Future work will focus on acquiring ultrasound data together with these measurements to better understand the impact of the respiratory cycle on the sliding velocity estimation. Another important note about the acquisition process is that focus was set at 2 cm and was not adjusted for the pleural depth of each patient or area. However, the median pleural depth in the two datasets is 2.35 cm, so the 2 cm focus is appropriate on average. Moreover, no correlation was observed between pleural depth and SlV values, implying that depth may not have a significant impact on the final velocity estimation. We also acknowledge that for a strong analysis, a control group with healthy subjects would be needed. Future work will focus on acquiring data from healthy subjects and incorporating them into the analysis. Finally, we want to highlight that the robustness, interpretability, and generalizability of this study are directly impacted by these limitations, which should be considered when interpreting the results. This is why the findings of this pilot study should be considered exploratory.

Nonetheless, the positive results obtained in this study highlight the capability of this methodology to characterize lung pathologies and suggest its possible impact on improving the diagnostic process.

5. Conclusion

This study introduces a novel methodology to estimate the velocity of pleural sliding, referred to as the sliding velocity. This novel methodology comprises a velocity model inspired by fUS. Indeed, this model relates the velocity represented in each pixel to the frequency components of the slow-time intensity signal. We conducted an experimental validation using a moving phantom with known velocity. The results demonstrated promising sensitivity to motion, highlighting however, the presence of a scaling factor that prevents interpretation of SIV as an absolute physical velocity. At the moment, it should therefore be considered an instrument-dependent biomarker.

We applied this novel methodology to two datasets of in-vivo LUS data. These datasets comprised RF multifrequency LUS videos acquired from patients affected by five respiratory pathologies: CPE, pneumonia, COPD, fibrosis, and exacerbated. The datasets were originally intended for static pattern analysis, and the relatively low frame rate may have introduced a saturation limiting the maximum estimable velocity. Future work will be focused on investigating the role played by the frame rate in our methodology and on establishing an optimal value for this parameter. Furthermore, the pivotal point of this saturation problem is the low value of the maximum estimable velocity, which depends not only on the frame rate but also on the lateral resolution. Therefore, further investigation will also focus on increasing this value through the use of plane-wave imaging.

Optimizing these parameters and implementing them in new datasets, which should include healthy subjects as well as a control group, may enable a more accurate characterization of the sliding velocity and may reveal further differences among different pathological populations. Overall, it is important to note that the findings of this study should be interpreted as exploratory, as the limitations affect its robustness, interpretability, and generalizability.

Finally, although this was a preliminary study, the results we obtained are promising. Indeed, the sliding velocity values were within the physiological range (≈0.49 mm/s - ≈ 4.39 mm/s), and different pathological populations showed statistically significant differences. These differences were also evident when these velocities were used to train and test binary classifiers, achieving an accuracy of up to 76.43% when differentiating between CPE and pneumonia, 83.82% when differentiating between CPE and COPD, 78.29% when differentiating between CPE and fibrosis, 85.19% when differentiating between CPE and fibrosis exacerbated, 94.06% when differentiating between COPD and pneumonia, 85.76% when differentiating between fibrosis and pneumonia, 87.20% when differentiating between fibrosis exacerbated and pneumonia, 77.18% when differentiating between fibrosis and COPD, 69.35% when differentiating between fibrosis exacerbated and COPD,

and 62.50% when differentiating between fibrosis and fibrosis exacerbated. However, it is important to note that the results of cross-dataset pairs may be influenced by other factors. Therefore, the results should be considered exploratory. The low accuracy and the lack of robustness of the classifiers when distinguishing between fibrosis and fibrosis exacerbated populations provide further evidence of the discriminative potential of the sliding velocity, considering that these two populations are indeed the same pathology but at different stages.

CRediT authorship contribution statement

Chiara Zangrandi: Writing – review & editing, Writing – original draft, Visualization, Validation, Methodology, Investigation, Conceptualization. **Federico Mento:** Writing – review & editing, Validation, Methodology, Investigation, Conceptualization. **Mattia Perpenti:** Writing – original draft, Validation, Investigation, Formal analysis. **Giovanni Pierro:** Data curation. **Alessandro Perrotta:** Data curation. **Tiziano Perrone:** Data curation. **Andrea Smargiassi:** Data curation. **Riccardo Inchingolo:** Data curation. **Libertario Demi:** Writing – review & editing, Validation, Supervision, Project administration, Methodology, Investigation, Formal analysis, Conceptualization.

Ethics approval

Data acquisition was carried out in accordance with the World Medical Association Declaration of Helsinki and was approved by the independent ethics committee for clinical studies of the IRCCS Clinical Institute Humanitas in Rozzano: protocol number 553/21 (LUSARD dataset), and by the Ethical Committee of the Fondazione Policlinico Universitario Gemelli IRCCS in Rome, protocol 0002865/22, ID 4710 (SAURON dataset).

Funding

This work was partially supported by a research grant provided in compliance with Mission 6/Component 2/Investment: 2.1 “Strengthening and enhancing biomedical research in the NHS”, financed by the European Union - NextGenerationEU, CUP: E63C24000660007.

Declaration of competing interest

The authors declare that they have no known competing financial interests or personal relationships that could have appeared to influence the work reported in this paper.

Appendix A. Statistical analysis results

In this appendix, the detailed results of the statistical analyses on the five pathological populations (cardiogenic pulmonary edema (CPE), pneumonia (PNE), chronic obstructive pulmonary disease (COPD), fibrosis (PF), and fibrosis exacerbated (PFE)) are presented in Tables A.4–A.8. For each case, the following metrics are reported for each frequency and each pathological pair: p-values, obtained from the mixed-effects model for Case 1 and from the Mann–Whitney test for the other cases; adjusted q-values, calculated using the FDR Benjamini–Hochberg method; effect sizes with their corresponding 95% CI. In each table, statistically significant p-values and q-values (<0.05) are highlighted in yellow. Moreover, the top part of each table reports the results of five pathological pairs (CPE-PNE, CPE-COPD, CPE-PF, CPE-PFE, PF-PFE), while the bottom part of the table reports the results of the other five pairs (PNE-COPD, PNE-PF, PNE-PFE, COPD-PF, COPD-PFE). Pairs of pathologies within the same dataset are indicated in bold.

Table A.4
Statistical analysis results for case 1- total data: p-values, q-values, effect sizes, and 95% CI across frequencies (3–6 MHz). Pairs of pathologies within the same dataset are indicated in bold.

CASE 1 - TOT						
Freq [MHz]		CPE vs COPD	CPE vs PF	CPE vs PFE	CPE vs PNE	PF vs PFE
3	p-value	< 0.001	0.238	0.053	0.284	0.313
	q-value	< 0.001	0.356	0.113	0.406	0.432
	Effect Size [CI]	−0.904 [−1.345 −0.464]	−0.263 [−0.699 0.173]	−0.475 [−0.954 0.005]	0.293 [−0.242 0.827]	−0.212 [−0.623 0.199]
4	p-value	0.001	0.245	0.026	0.285	0.171
	q-value	0.003	0.360	0.062	0.404	0.287
	Effect Size [CI]	−0.754 [−1.186 −0.321]	−0.254 [−0.682 0.174]	−0.536 [−1.007 −0.065]	0.290 [−0.241 0.822]	−0.282 [−0.685 0.121]
5	p-value	0.002	0.173	0.012	0.631	0.136
	q-value	0.009	0.286	0.033	0.734	0.238
	Effect Size [CI]	−0.664 [−1.089 −0.239]	−0.294 [−0.717 0.128]	−0.594 [−1.057 −0.131]	0.129 [−0.398 0.657]	−0.299 [−0.692 0.093]
6	p-value	0.051	0.256	0.018	0.225	0.111
	q-value	0.109	0.374	0.046	0.343	0.206
	Effect Size [CI]	−0.425 [−0.851 0.001]	−0.245 [−0.667 0.177]	−0.558 [−1.019 −0.098]	0.329 [−0.202 0.860]	−0.313 [−0.698 0.072]
		PNE vs COPD	PNE vs PF	PNE vs PFE	COPD vs PF	COPD vs PFE
3	p-value	< 0.001	0.022	0.004	0.001	0.044
	q-value	< 0.001	0.054	0.013	0.003	0.097
	Effect Size [CI]	−1.197 [−1.675 −0.718]	−0.555 [−1.029 −0.081]	−0.767 [−1.282 −0.253]	0.642 [0.276 1.007]	0.430 [0.013 0.846]
4	p-value	<0.001	0.024	0.002	0.006	0.296
	q-value	0.001	0.059	0.006	0.019	0.416
	Effect Size [CI]	−1.044 [−1.520 −0.568]	−0.544 [−1.017 −0.072]	−0.826 [−1.338 −0.315]	0.499 [0.142 0.856]	0.218 [−0.190 0.625]
5	p-value	<0.001	0.076	0.005	0.037	0.727
	q-value	0.004	0.152	0.016	0.084	0.812
	Effect Size [CI]	−0.793 [−1.263 −0.324]	−0.423 [−0.890 0.044]	−0.723 [−1.227 −0.219]	0.370 [0.023 0.717]	0.071 [−0.325 0.466]
6	p-value	0.002	0.016	0.001	0.303	0.502
	q-value	0.007	0.043	0.003	0.424	0.628
	Effect Size [CI]	−0.754 [−1.224 −0.284]	−0.574 [−1.041 −0.107]	−0.887 [−1.389 −0.386]	0.180 [−0.162 0.523]	−0.133 [−0.522 0.256]

Table A.5
Statistical analysis results for case 2- Mean: p-values, q-values, effect sizes, and 95% CI across frequencies (3–6 MHz). Pairs of pathologies within the same dataset are indicated in bold.

CASE 2 - MEAN						
Freq [MHz]		CPE vs COPD	CPE vs PF	CPE vs PFE	CPE vs PNE	PF vs PFE
3	p-value	0.001	0.205	0.097	0.394	0.533
	q-value	0.003	0.323	0.185	0.522	0.659
	Effect Size [CI]	0.691 [0.448 0.934]	0.253 [−0.067 0.574]	0.378 [0.029 0.727]	0.190 [−0.174 0.553]	0.133 [−0.210 0.477]
4	p-value	<0.001	0.194	0.118	0.222	0.484
	q-value	0.003	0.312	0.215	0.342	0.608
	Effect Size [CI]	0.705 [0.467 0.944]	0.260 [−0.060 0.580]	0.356 [0.003 0.708]	0.272 [−0.085 0.628]	0.150 [−0.193 0.493]
5	p-value	<0.001	0.172	0.036	0.394	0.228
	q-value	0.005	0.286	0.082	0.519	0.345
	Effect Size [CI]	0.656 [0.402 0.910]	0.273 [−0.045 0.592]	0.478 [0.146 0.809]	0.190 [−0.174 0.553]	0.258 [−0.076 0.593]
6	p-value	0.003	0.230	0.022	0.069	0.186
	q-value	0.012	0.346	0.054	0.139	0.302
	Effect Size [CI]	0.593 [0.322 0.864]	0.240 [−0.082 0.562]	0.522 [0.201 0.844]	0.405 [0.066 0.744]	0.283 [−0.049 0.616]
		PNE vs COPD	PNE vs PF	PNE vs PFE	COPD vs PF	COPD vs PFE
3	p-value	<0.001	0.033	0.012	0.004	0.133
	q-value	0.002	0.076	0.033	0.012	0.240
	Effect Size [CI]	0.781 [0.565 0.998]	0.446 [0.141 0.752]	0.590 [0.273 0.906]	0.542 [0.278 0.806]	0.325 [−0.008 0.658]
4	p-value	<0.001	0.010	0.017	0.005	0.209
	q-value	0.001	0.028	0.043	0.017	0.324
	Effect Size [CI]	0.895 [0.740 1.049]	0.538 [0.251 0.826]	0.564 [0.240 0.888]	0.521 [0.253 0.789]	0.272 [−0.067 0.611]
5	p-value	<0.001	0.047	0.011	0.035	0.626
	q-value	0.001	0.101	0.029	0.081	0.741
	Effect Size [CI]	0.806 [0.600 1.011]	0.415 [0.105 0.726]	0.603 [0.290 0.915]	0.395 [0.106 0.683]	0.105 [−0.245 0.455]
6	p-value	<0.001	0.012	<0.001	0.144	0.871
	q-value	0.001	0.034	0.003	0.248	0.942
	Effect Size [CI]	0.822 [0.624 1.019]	0.523 [0.232 0.814]	0.821 [0.596 1.045]	0.274 [−0.028 0.576]	0.035 [−0.317 0.387]

Table A.6
Statistical analysis results for case 3- Min: p-values, q-values, effect sizes, and 95% CI across frequencies (3–6 MHz). Pairs of pathologies within the same dataset are indicated in bold.

CASE 3 - MIN						
Freq [MHz]		CPE vs COPD	CPE vs PF	CPE vs PFE	CPE vs PNE	PF vs PFE
3	p-value	0.001	0.004	0.010	0.134	0.876
	q-value	0.004	0.013	0.028	0.240	0.942
	Effect Size [CI]	0.663 [0.412 0.915]	0.573 [0.302 0.845]	0.589 [0.284 0.894]	0.333 [−0.016 0.683]	0.033 [−0.313 0.380]
4	p-value	0.001	0.008	0.019	0.084	0.815
	q-value	0.004	0.025	0.049	0.163	0.901
	Effect Size [CI]	0.670 [0.421 0.920]	0.527 [0.245 0.808]	0.533 [0.214 0.852]	0.385 [0.043 0.727]	0.050 [−0.296 0.396]
5	p-value	<0.001	0.004	0.003	0.369	0.312
	q-value	0.001	0.012	0.012	0.499	0.433
	Effect Size [CI]	0.754 [0.534 0.975]	0.580 [0.310 0.850]	0.667 [0.386 0.948]	0.200 [−0.163 0.563]	0.217 [−0.122 0.555]
6	p-value	<0.001	0.021	0.002	0.160	0.243
	q-value	0.001	0.054	0.009	0.274	0.360
	Effect Size [CI]	0.775 [0.563 0.988]	0.460 [0.166 0.754]	0.689 [0.415 0.962]	0.313 [−0.039 0.665]	0.250 [−0.085 0.585]
		PNE vs COPD	PNE vs PF	PNE vs PFE	COPD vs PF	COPD vs PFE
3	p-value	<0.001	<0.001	<0.001	0.933	0.935
	q-value	0.001	0.001	0.001	0.972	0.969
	Effect Size [CI]	0.903 [0.754 1.052]	0.800 [0.595 1.005]	0.910 [0.748 1.073]	0.016 [−0.298 0.330]	0.018 [−0.334 0.370]
4	p-value	<0.001	<0.001	<0.001	0.574	0.968
	q-value	<0.001	<0.001	0.005	0.696	0.987
	Effect Size [CI]	0.976 [0.900 1.052]	0.838 [0.653 1.024]	0.769 [0.519 1.020]	0.105 [−0.207 0.417]	0.009 [−0.343 0.361]
5	p-value	<0.001	<0.001	<0.001	0.399	0.516
	q-value	<0.001	0.003	0.002	0.522	0.642
	Effect Size [CI]	0.895 [0.740 1.049]	0.738 [0.508 0.969]	0.885 [0.702 1.067]	0.158 [−0.152 0.468]	0.140 [−0.208 0.489]
6	p-value	<0.001	<0.001	<0.001	0.694	0.194
	q-value	<0.001	0.003	0.002	0.789	0.311
	Effect Size [CI]	0.919 [0.782 1.056]	0.708 [0.467 0.949]	0.872 [0.680 1.064]	0.074 [−0.239 0.387]	0.281 [−0.057 0.619]

Table A.7
Statistical analysis results for case 4- Max: p-values, q-values, effect sizes, and 95% CI across frequencies (3–6 MHz). Pairs of pathologies within the same dataset are indicated in bold.

CASE 4 - MAX						
Freq [MHz]		CPE vs COPD	CPE vs PF	CPE vs PFE	CPE vs PNE	PF vs PFE
3	p-value	0.435	0.271	0.329	0.596	0.907
	q-value	0.561	0.390	0.451	0.718	0.965
	Effect Size	0.158	0.220	0.222	0.118	0.025
	[CI]	[−0.174 0.490]	[−0.103 0.543]	[−0.146 0.590]	[−0.250 0.486]	[−0.321 0.371]
4	p-value	0.456	0.067	0.354	0.565	0.815
	q-value	0.577	0.136	0.481	0.693	0.896
	Effect Size	0.151	0.367	0.211	0.128	0.050
	[CI]	[−0.181 0.483]	[0.058 0.675]	[−0.158 0.580]	[−0.239 0.496]	[−0.296 0.396]
5	p-value	0.665	0.057	0.380	0.629	0.111
	q-value	0.760	0.118	0.510	0.735	0.207
	Effect Size	0.088	0.380	0.200	0.108	0.342
	[CI]	[−0.247 0.423]	[0.074 0.686]	[−0.170 0.570]	[−0.261 0.476]	[0.016 0.667]
6	p-value	0.160	0.117	0.143	0.259	0.938
	q-value	0.271	0.215	0.249	0.375	0.967
	Effect Size	0.284	0.313	0.333	0.251	0.017
	[CI]	[−0.038 0.606]	[−0.001 0.628]	[−0.022 0.689]	[−0.107 0.610]	[−0.330 0.363]
		PNE vs COPD	PNE vs PF	PNE vs PFE	COPD vs PF	COPD vs PFE
3	p-value	0.409	0.658	0.786	0.077	0.105
	q-value	0.532	0.757	0.873	0.152	0.198
	Effect Size	0.174	0.092	0.064	0.332	0.351
	[CI]	[−0.167 0.515]	[−0.247 0.432]	[−0.327 0.455]	[0.035 0.628]	[0.021 0.681]
4	p-value	0.954	0.077	0.384	0.031	0.209
	q-value	0.979	0.151	0.512	0.072	0.326
	Effect Size	0.012	0.369	0.205	0.405	0.272
	[CI]	[−0.334 0.359]	[0.052 0.686]	[−0.179 0.589]	[0.118 0.692]	[−0.067 0.611]
5	p-value	0.631	0.047	0.446	0.056	0.903
	q-value	0.730	0.103	0.572	0.117	0.966
	Effect Size	0.101	0.415	0.179	0.358	0.026
	[CI]	[−0.243 0.446]	[0.105 0.726]	[−0.206 0.565]	[0.065 0.651]	[−0.326 0.378]
6	p-value	0.985	1.000	0.913	0.866	0.968
	q-value	0.995	1.000	0.956	0.941	0.982
	Effect Size	0.004	0.000	0.026	0.032	0.009
	[CI]	[−0.342 0.351]	[−0.341 0.341]	[−0.366 0.418]	[−0.282 0.345]	[−0.343 0.361]

Table A.8
Statistical analysis results for case 5- Delta: p-values, q-values, effect sizes, and 95% CI across frequencies (3–6 MHz). Pairs of pathologies within the same dataset are indicated in bold.

CASE 5 - DELTA						
Freq [MHz]		CPE vs COPD	CPE vs PF	CPE vs PFE	CPE vs PNE	PF vs PFE
3	p-value	0.008	0.004	0.008	0.093	0.846
	q-value	0.024	0.013	0.025	0.178	0.924
	Effect Size [CI]	0.537 [0.253 0.820]	0.580 [0.310 0.850]	0.600 [0.298 0.902]	0.374 [0.031 0.718]	0.042 [−0.305 0.388]
4	p-value	0.001	0.004	0.010	0.056	0.907
	q-value	0.004	0.013	0.028	0.118	0.960
	Effect Size [CI]	0.670 [0.421 0.920]	0.580 [0.310 0.850]	0.589 [0.284 0.894]	0.426 [0.090 0.761]	0.025 [−0.321 0.371]
5	p-value	<0.001	0.001	0.001	0.134	0.613
	q-value	0.002	0.004	0.005	0.238	0.734
	Effect Size [CI]	0.740 [0.514 0.966]	0.667 [0.420 0.914]	0.733 [0.477 0.990]	0.333 [−0.016 0.683]	0.108 [−0.236 0.453]
6	p-value	<0.001	0.001	<0.001	0.565	0.173
	q-value	0.002	0.004	0.002	0.689	0.284
	Effect Size [CI]	0.761 [0.543 0.979]	0.667 [0.420 0.914]	0.811 [0.590 1.032]	0.128 [−0.239 0.496]	0.292 [−0.040 0.623]
		PNE vs COPD	PNE vs PF	PNE vs PFE	COPD vs PF	COPD vs PFE
3	p-value	<0.001	<0.001	<0.001	0.448	0.626
	q-value	<0.001	<0.001	<0.001	0.571	0.746
	Effect Size [CI]	0.862 [0.687 1.038]	0.900 [0.751 1.049]	0.936 [0.798 1.074]	0.142 [−0.169 0.453]	0.105 [−0.245 0.455]
4	p-value	<0.001	<0.001	<0.001	0.911	0.715
	q-value	<0.001	<0.001	0.003	0.958	0.803
	Effect Size [CI]	0.927 [0.797 1.057]	0.846 [0.664 1.028]	0.821 [0.596 1.045]	0.021 [−0.293 0.335]	0.079 [−0.272 0.430]
5	p-value	<0.001	<0.001	<0.001	1.000	0.626
	q-value	<0.001	<0.001	<0.001	1.005	0.737
	Effect Size [CI]	0.887 [0.726 1.047]	0.846 [0.664 1.028]	0.885 [0.702 1.067]	0.000 [−0.314 0.314]	0.105 [−0.245 0.455]
6	p-value	<0.001	0.001	<0.001	0.715	0.194
	q-value	<0.001	0.003	0.003	0.808	0.309
	Effect Size [CI]	0.789 [0.577 1.002]	0.715 [0.477 0.954]	0.833 [0.617 1.050]	0.068 [−0.245 0.382]	0.281 [−0.057 0.619]

Appendix B. Confusion matrices

In this appendix, the confusion matrices obtained from the binary classification are reported. Specifically, each pathological pair is characterized by the confusion matrix (or confusion matrices in the case of equal accuracy) corresponding to the classifier and center frequency at which the pair achieved the highest accuracy. Each confusion matrix is computed as the mean of the 10 confusion matrices (one for each repetition) and then normalized by the sample size of the corresponding pathology. Pairs of pathologies within the same dataset are indicated in red.

Fig. B.12 shows the confusion matrices for the pathological pair PF-PFE, where PF stands for fibrosis, and PFE for fibrosis exacerbated. Specifically, three confusion matrices are shown since the pair reported the same accuracy (62.5%) at 3 MHz and at 4 MHz with a SVM classifier and at 5 MHz with a DT classifier. Fig. B.13 shows the confusion matrices for six pathological pairs: CPE-PNE, CPE-COPD, CPE-PF, CPE-PFE, COPD-PF, and COPD-PFE, where CPE stands for cardiogenic pulmonary edema, PNE for pneumonia, COPD for chronic obstructive pulmonary disease, PF for fibrosis, and PFE for fibrosis exacerbated. Fig. B.14 shows the confusion matrices for three pathological pairs: PNE-COPD, PNE-PF, and PNE-PFE. The pair PNE-PFE has two different confusion matrices since it reported the same accuracy (87.2%) at 4 MHz with an SVM classifier and at 6 MHz with a KNN classifier.

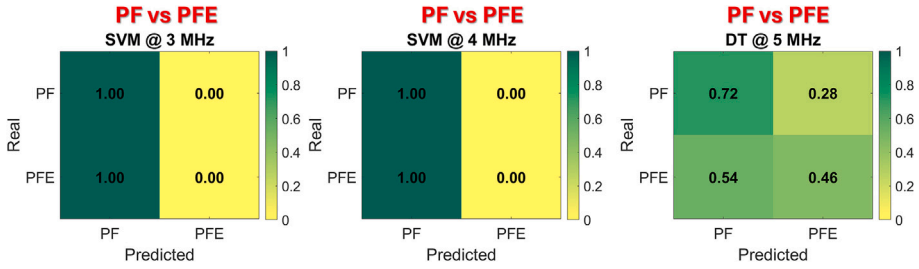

Fig. B.12. This figure presents the confusion matrices for the pathological pair PF-PFE. Specifically, three confusion matrices are displayed since the pair achieved the same accuracy (62.5%) at 3 MHz and at 4 MHz with an SVM classifier and at 5 MHz with a DT classifier. In the title of each confusion matrix, the pathological pair is indicated along with the classifier name and the center frequency at which it achieved the best accuracy. Pairs of pathologies within the same dataset are highlighted in red.

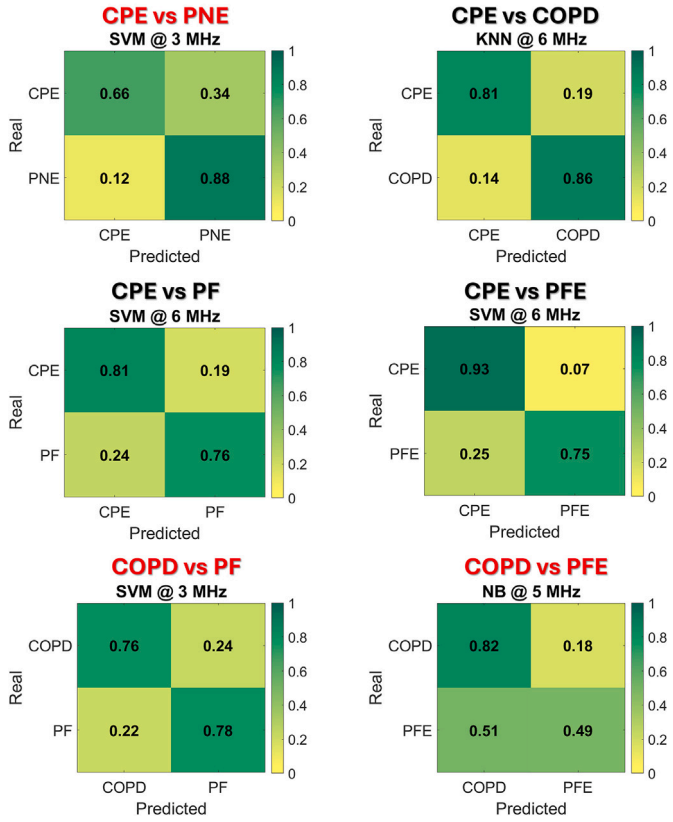

Fig. B.13. This figure presents the confusion matrix for six pathological pairs: CPE-PNE, CPE-COPD, CPE-PF, CPE-PFE, COPD-PF, and COPD-PFE. In the title of each confusion matrix, the pathological pair is displayed along with the classifier name and the center frequency at which it achieved the best accuracy. Pairs of pathologies within the same dataset are highlighted in red.

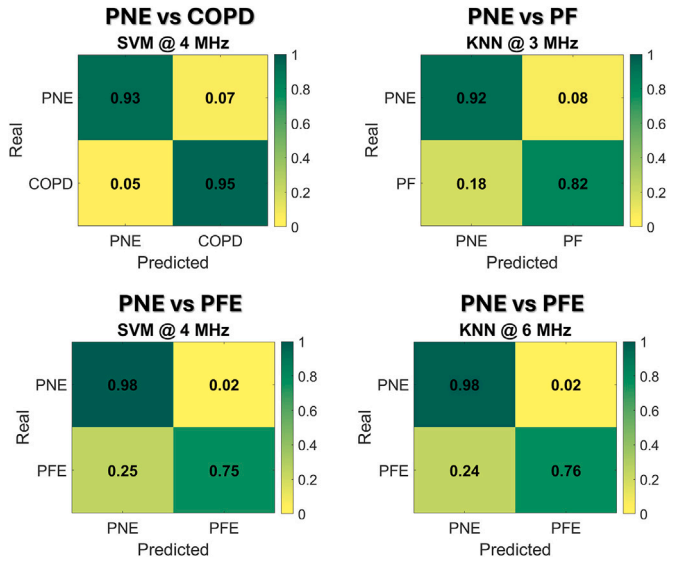

Fig. B.14. This figure presents the confusion matrix for three pathological pairs: PNE-COPD, PNE-PF, and PNE-PFE. The pair PNE-PFE has two distinct confusion matrices since it achieved the same accuracy (87.2%) at 4 MHz with an SVM classifier and at 6 MHz with a KNN classifier. In the title of each confusion matrix, the pathological pair is indicated along with the classifier name and the center frequency at which it achieved the best accuracy.

Appendix C. ROC curves and AUC values

This appendix reports, for each pathological pair, the ROC curves and AUC values of the configuration (classifier, center frequency, and feature combination) that achieves the highest mean accuracy. The ROC curves and AUC values were obtained using the $perfcurve$ function in MATLAB. Pairs of pathologies within the same dataset are indicated in red.

Fig. C.15 shows the ROC curves for four pathological pairs: CPE-PNE, CPE-COPD, CPE-PF, and CPE-PFE, where CPE stands for cardiogenic pulmonary edema, PNE for pneumonia, COPD for chronic obstructive pulmonary disease, PF for fibrosis, and PFE for fibrosis exacerbated. Fig. C.16 shows the confusion matrices for six pathological pairs: PNE-COPD, PNE-PF, PNE-PFE, COPD-PF, COPD-PFE, and PF-PFE. AUC values are reported numerically in the title of each plot.

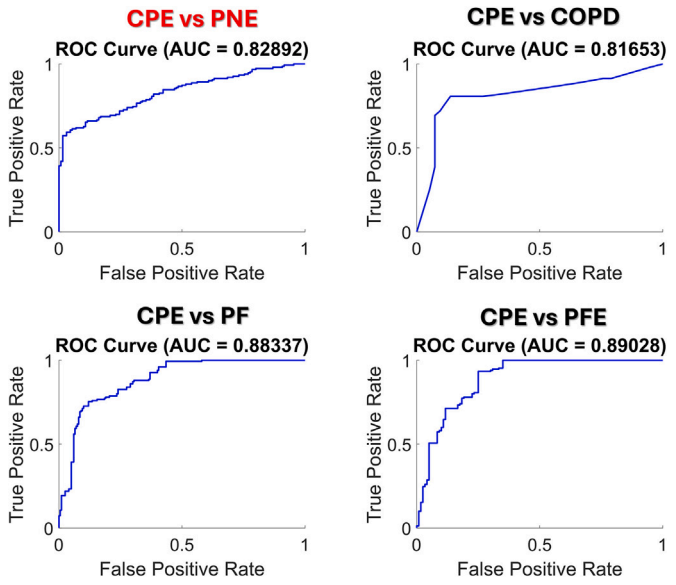

Fig. C.15. This figure shows the ROC curves for four pathological pairs: CPE-PNE, CPE-COPD, CPE-PF, and CPE-PFE. AUC values are reported numerically in the title of each plot. Pairs of pathologies within the same dataset are indicated in red.

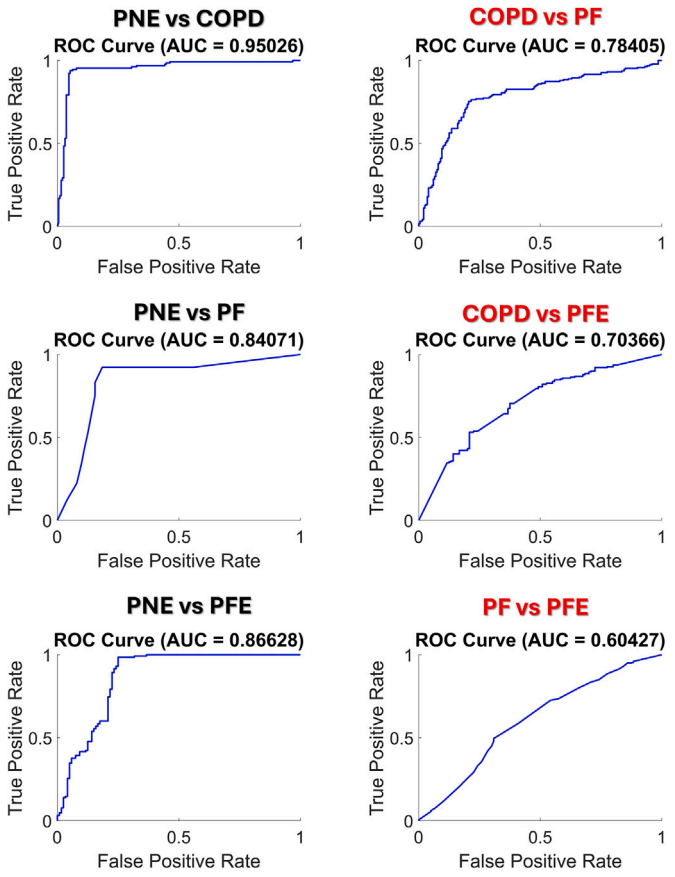

Fig. C.16. This figure shows the confusion matrices for six pathological pairs: PNE-COPD, PNE-PF, PNE-PFE, COPD-PF, COPD-PFE, and PF-PFE. AUC values are reported numerically in the title of each plot. Pairs of pathologies within the same dataset are indicated in red.

References

[1] F. Mento, U. Khan, F. Faita, A. Smargiassi, R. Inchingolo, T. Perrone, L. Demi, State of the art in lung ultrasound, shifting from qualitative to quantitative analyses, Ultrasound Med. Biol. 48 (12) (2022) 2398–2416, https://doi.org/10.1016/j.ultrasmedbio.2022.07.007, https://www.sciencedirect.com/science/article/pii/S0301562922004823.

[2] L. Demi, F. Wolfram, C. Klersy, A. De Silvestri, V.V. Ferretti, M. Muller, D. Miller, F. Feletti, M. Wełnicki, N. Buda, A. Skoczylas, A. Pomiecko, D. Damjanovic, R. Olszewski, A.W. Kirkpatrick, R. Breitkreutz, G. Mathis, G. Soldati, A. Smargiassi, R. Inchingolo, T. Perrone, New international guidelines and consensus on the use of lung ultrasound, J. Ultrasound Med. 42 (2) (2023) 309–344, _eprint: https://doi.org/10.1002/jum.16088.

[3] L. Demi, T. Egan, M. Muller, Lung ultrasound imaging, a technical review, Appl. Sci. 10 (2) (2020) 462, number: 2 Publisher: Multidisciplinary Digital Publishing Institute. https://doi.org/10.3390/app10020462.

[4] F. Mento, M. Perpenti, G. Barcellona, T. Perrone, L. Demi, Lung ultrasound spectroscopy applied to the differential diagnosis of pulmonary diseases: an in vivo multicenter clinical study, IEEE Trans. Ultrason. Ferroelectr. Freq. Control 71 (10) (2024) 1217–1232, conference Name: IEEE Transactions on Ultrasonics, Ferroelectrics, and Frequency Control. https://doi.org/10.1109/TUFFC.2024.3454956, https://ieeexplore.ieee.org/document/10666733/authors#authors.

[5] M. Perpenti, F. Mento, G. Pierro, A. Perrotta, T. Perrone, A. Smargiassi, R. Inchingolo, L. Demi, Fully automated quantitative lung ultrasound spectroscopy for the differential diagnosis of lung diseases: the first multicenter in-vivo clinical study, Comput. Biol. Med. 200 (2026) 111365, https://doi.org/10.1016/j.compbiomed.2025.111365, https://www.sciencedirect.com/science/article/pii/S0010482525017196.

[6] R. Inchingolo, A. Zanforlin, D. Buonsenso, T. Perrone, E. Torri, G. Limoli, E.E. Mossolani, F. Tursi, G. Soldati, G. Marchetti, P. Carlucci, D. Radovanovic, F.M. Lohmeyer, A. Smargiassi, Lung ultrasound signs, J. Ultrasound Med. 43 (4) (2024) 629–641, _eprint: https://doi.org/10.1002/jum.16397

[7] D.N. Briganti, C.E. Choi, J. Nguyen, C.W. Lanks, Determinants of point-of-care ultrasound lung sliding amplitude in mechanically ventilated patients, Ultrasound J. 15 (1) (2023) 25, https://doi.org/10.1186/s13089-023-00326-5

[8] D.A. Lichtenstein, Y. Menu, A bedside ultrasound sign ruling out pneumothorax in the critically III: lung sliding, Chest 108 (5) (1995) 1345–1348, https://doi.org/10.1378/chest.108.5.1345, https://www.sciencedirect.com/science/article/pii/S0012369216357130.

[9] G. Via, E. Storti, G. Gulati, L. Neri, F. Mojoli, A. Braschi, Lung ultrasound in the ICU: from diagnostic instrument to respiratory monitoring tool, Minerva Anestesiol. 78 (11) (2012) 1282–1296.

[10] D.A. Lichtenstein, Lung ultrasound (in the critically ill) superior to CT: the example of lung sliding, Korean J Crit Care Med 32 (1) (2017) 1–8, publisher: Korean Society of Critical Care Medicine. https://doi.org/10.4266/kjccm.2016.00955, https://synapse.koreamed.org/articles/1154058.

[11] I. Şirin, A.B. Erdem, C.B. Uysal, C. Gedikaslan, The effect of tidal volumes of mechanically ventilated patients on lung sliding amplitude in Point-Of-Care lung ultrasound, J. Clin. Ultrasound 53 (5) (2025) 989–996, _eprint: https://doi.org/10.1002/jcu.23968.

[12] G. Rose, S. Siadecki, R. Tansek, N. Baranchuk, T. Saul, A novel method of assessing for lung sliding using Doppler imaging, Am. J. Emerg. Med. 35 (11) (2017) 1738–1742, https://doi.org/10.1016/j.ajem.2017.09.006, https://www.sciencedirect.com/science/article/pii/S0735675717307337.

[13] R. Xiao, Q. Shao, N. Zhao, F. Liu, K.-J. Qian, Quantification analysis of pleural line movement for the diagnosis of pneumothorax, World J. Clin. Cases 9 (21) (2021) 5889–5899, https://doi.org/10.12998/wjcc.v9.i21.5889, https://pmc.ncbi.nlm.nih.gov/articles/PMC8316966/.

[14] G. Duclos, X. Bobbia, T. Markarian, L. Muller, C. Cheyssac, S. Castillon, N. Resseguier, A. Boussuges, G. Volpicelli, M. Leone, L. Zieleskiewicz, Speckle tracking quantification of lung sliding for the diagnosis of pneumothorax: a multicentric observational study, Intensive Care Med. 45 (9) (2019) 1212–1218, https://doi.org/10.1007/s00134-019-05710-1

[15] E. Fissore, L. Zieleskiewicz, T. Markarian, L. Muller, G. Duclos, M. Bourgoin, P. Michelet, M. Leone, P.-G. Claret, X. Bobbia, Pneumothorax diagnosis with lung sliding quantification by speckle tracking: a prospective multicentric observational study, Am. J. Emerg. Med. 49 (2021) 14–17, https://doi.org/10.1016/j.ajem.2021.05.022, https://www.sciencedirect.com/science/article/pii/S0735675721003983.

[16] G. Duclos, L. Marecal, N. Resseguier, M. Postzich, C. Taguet, S. Hraiech, M. Leone, L. Müller, L. Zieleskiewicz, Pleural lung sliding quantification using a speckle tracking technology: a feasibility study on 30 healthy volunteers, Comput. Methods Programs Biomed. 254 (2024) 108316, https://doi.org/10.1016/j.cmpb.2024.108316, https://www.sciencedirect.com/science/article/pii/S0169260724003092.

[17] B. Tzadok, Y. Blumberg, M. Shubert, M. Halabi, E. Tal-Or, N. Bachner-Hinenzon, S. Carasso, Speckled tracking of pleura—a novel tool for lung ultrasound; distinguishing COVID-19 from acute heart failure, J. Clin. Med. 11 (16) (2022) 4846, number: 16 Publisher: Multidisciplinary Digital Publishing Institute. https://doi.org/10.3390/jcm11164846.

[18] G. Dori, D.J. Jakobson, Speckle tracking technology for quantifying lung sliding, Med. Hypotheses 91 (2016) 81–83, https://doi.org/10.1016/j.mehy.2016.04.019, https://linkinghub.elsevier.com/retrieve/pii/S0306987716300366.

[19] M. Jaščur, M. Bundzel, M. Malík, A. Dzian, N. Ferenčí, F. Babič, Detecting the absence of lung sliding in lung ultrasounds using deep learning, Appl. Sci. 11 (15) (2021) 6976, publisher: Multidisciplinary Digital Publishing Institute. https://doi.org/10.3390/app11156976.

[20] B. VanBerlo, D. Wu, B. Li, M.A. Rahman, G. Hogg, B. VanBerlo, J. Tschirhart, A. Ford, J. Ho, J. McCauley, B. Wu, J. Deglint, J. Hargun, R. Chaudhary, C. Dave, R. Arntfield, Accurate assessment of the lung sliding artefact on lung ultrasonography using a deep learning approach, Comput. Biol. Med. 148 (2022) 105953, https://doi.org/10.1016/j.compbiomed.2022.105953, https://www.sciencedirect.com/science/article/pii/S0010482522006849.

[21] E. Macé, G. Montaldo, I. Cohen, M. Baulac, M. Fink, M. Tanter, Functional ultrasound imaging of the brain, Nat. Methods 8 (8) (2011) 662–664, https://doi.org/10.1038/nmeth.1641.

[22] Q. Zheng, I.A. Cox, J.A. Campbell, Q. Xia, P. Otahal, B. de Graaff, T.J. Corte, A.K.Y. Teoh, E.H. Walters, A.J. Palmer, Mortality and survival in idiopathic pulmonary fibrosis: a systematic review and meta-analysis, ERJ Open Res. 8 (1) (2022) 00591–2021, https://doi.org/10.1183/23120541.00591-2021

[23] M.M. Juarez, A.L. Chan, A.G. Norris, B.M. Morrissey, T.E. Albertson, Acute exacerbation of idiopathic pulmonary fibrosis—a review of current and novel pharmacotherapies, J. Thorac. Dis. 7 (3), publisher: AME Publishing Company. 2025, https://doi.org/10.3978/j.issn.2072-1439.2015.01.17, https://jtd.amegroups.org/article/view/4140.

[24] The top 10 causes of death, https://www.who.int/news-room/fact-sheets/detail/the-top-10-causes-of-death.

[25] P. Tortoli, L. Bassi, E. Boni, A. Dallai, F. Guidi, S. Ricci, ULA-OP: an advanced open platform for ultrasound research, IEEE Trans. Ultrason. Ferroelectr. Freq. Control 56 (10) (2009) 2207–2216, conference Name: IEEE Transactions on Ultrasonics, Ferroelectrics, and Frequency Control. https://doi.org/10.1109/TUFFC.2009.1303, https://ieeexplore.ieee.org/document/5306767/?arnumber=5306767.

[26] G. Soldati, A. Smargiassi, R. Inchingolo, D. Buonsenso, T. Perrone, D.F. Briganti, S. Perlini, E. Torri, A. Mariani, E.E. Mossolani, F. Tursi, F. Mento, L. Demi, Proposal for international standardization of the use of lung ultrasound for patients with COVID-19, J. Ultrasound Med. 39 (7) (2020) 1413–1419, _eprint: https://doi.org/10.1002/jum.15285.

[27] F. Mento, T. Perrone, A. Fiengo, F. Tursi, V.N. Macioce, A. Smargiassi, R. Inchingolo, L. Demi, Limiting the areas inspected by lung ultrasound leads to an underestimation of COVID-19 patients' condition, Intensive Care Med. 47 (7) (2021) 811–812, https://doi.org/10.1007/s00134-021-06407-0

[28] F. Mento, M. Perini, C. Malacarne, L. Demi, Ultrasound multifrequency strategy to estimate the lung surface roughness, *in silico* and *in vitro* results, Ultrasonics 135 (2023) 107143, https://doi.org/10.1016/j.ultras.2023.107143, https://www.sciencedirect.com/science/article/pii/S0041624X23002196.

[29] S.S. Shapiro, M.B. Wilk, An analysis of variance test for normality (complete samples), Biometrika 52 (3/4) (1965) 591–611.

[30] H.B. Mann, D.R. Whitney, On a test of whether one of two random variables is stochastically larger than the other, Ann. Math. Statist. 18 (1) (1947) 50–60.